Faculty of Physics
Institute of Astrophysics

Characterization of molecular gas substructures in the protoplanetary disk HD 163296 using ALMA interferometric data.

A thesis presented for the degree of
Master of Science in Astrophysics

Michel Yan Luis Maluenda Berna

Advisor : PhD. Viviana Guzmán
Evaluation Committee : PhD. Laura Pérez
PhD. Cristóbal Petrovich

Santiago, Chile
January 26, 2024

Acknowledgements

I would like to express my deepest gratitude to my parents, whose unwavering support and love have been the cornerstone of my journey. This work is not only a reflection of my efforts but also a testament to the sacrifices and encouragement they have provided me throughout my life.

To my mother, for her infinite patience, understanding, and the countless ways she has shown her love and support. Your belief in me, no matter how big or small my goals, has been a source of strength and inspiration. Your wisdom and kindness have shaped me in ways that words can hardly express.

To my father, for instilling in me the values of perseverance and hard work. Your example of resilience and dedication in the face of the most complex challenges has been a benchmark in my academic and personal life.

I also wish to express my deep gratitude to my advisor Viviana Guzmán, whose guidance and expertise have been instrumental in the realization of this research. Her feedback and academic rigor have not only shaped this investigation but have also significantly contributed to my professional growth.

Finally, I thank my family, siblings, and friends for the support they have given me throughout these years of study. Also, I am grateful to the institutions that have assisted me with funding, such as the NRAO and IA.

Abstract

This thesis presents a comprehensive study of the molecular gas substructures, specifically HCN and C_2H, in the protoplanetary disk HD 163296. Using interferometric data from ALMA in two rotational transitions (at 3 mm and 1 mm), which can resolve structures down to scales of 10 au, our research focuses on characterizing the gas substructures and comparing them with the millimeter dust in the protoplanetary disk around the HD 163296 star.

We employed a rigorous methodology to accurately characterize the general structure of the disk and its bright line emission rings, exploring the vertical and radial distribution of small molecules and comparing molecular lines with the dust continuum emission. This methodology included parameterizing the relative abundance of HCN and C_2H as a power law and incorporating Gaussian functions to model the observed bright ring substructures. We fitted the model parameters of the disk structure using MCMC analysis.

For the general structure of the disk, we analyzed where the vertical emission of HCN and C_2H originates from. To achieve greater accuracy in calculating the disk height, we used both sets of data, bands 3 (3mm) and 6 (1mm). The distribution of the molecules' emission follows a trend that can be extrapolated to other frequencies. We took advantage of both the difference in the energies of the upper levels and the angular resolution between these bands. The best model determined that the vertical emission comes from a height of $Z/R = 0.11$ for HCN, and $Z/R = 0.068$ for C_2H, that is close to the disk midplane.

Our study reveals the presence of 3 bright line emission rings within the molecular gas for the molecules HCN and C_2H. For HCN, the inner ring is located at 46.7 au from the central star, the second ring is situated at 118.3 au, and the third ring is located at 309.98 au. For C_2H, the inner ring is located at 46 au, the second ring is at 118 au, and the third ring is at 385 au. We discovered a high abundance of HCN and C_2H in the inner disk of HD 163296 (<150 au), which reached a peak of relative abundance of $\sim 6.8 \times 10^{-11}$ in the first ring for HCN (46.7 au), and $\sim 5.0 \times 10^{-11}$ for C_2H in the second ring (118 au), suggesting more active organic chemistry or the possibility of molecular emissions hidden in the ice of the outer disk.

The results indicate no universal connection between dust and molecular substructures. We found a significant overlap between dust and chemical substructures within 150 au, but this connection diminishes in the outer regions of the disk. The outermost bright rings of HCN and C_2H, located at approximately 309 and 385 au respectively, do not show correlation with the CO substructures, challenging the conventional understanding of the composition and dynamics of protoplanetary disks. The chemical conversion of CO into other species provides a partial explanation for the observed vertical substructures and the high C/O ratios needed for the abundance of C_2H and HCN. This work deepens our understanding of the complex dynamics and chemical processes in protoplanetary disks, offering valuable insights for future research in planet formation.

Contents

List of Tables

List of Figures

Chapter 1

Introduction

The most common way to observe a disk around a star is through the continuum emission of the hot dust. The excess emission in IR wavelengths is usually related to the presence of disks around young stars. The material around young stars forms these protoplanetary disks, eventually, this material will be incorporated on planets in formation, accreted by the central star, or blown out by stellar winds. Whatever the case, the chemistry composition of future planets depends on components that form into protoplanetary disks. Some of the molecules that were formed in protoplanetary disks are used as gas tracers of different elements like Carbon, Oxygen, or Nitrogen.

1.1 Formation of Protoplanetary disks

Protoplanetary disks are crucial for the formation of planets, they emerge around young stars during the process of star formation. The process begins with the gravitational collapse of a molecular cloud, forming a proto-star at its center. Molecular clouds are vast, cold, and dense clouds primarily composed of molecular hydrogen (Dobbs et al. (2014)) with traces of other elements and molecules. Molecular clouds are where star formation occurs.

Molecular clouds, the birthplaces of stars, contain distinct regions with key roles in star formation. "Clumps" or "clusters" are denser regions within these clouds, typically spanning about 1 parsec in size (Sadavoy et al. (2014)). Their higher density makes them favorable sites for star formation, as gravity is more likely to initiate the collapse needed for proto-star formation.

"Filaments" are narrow, elongated structures commonly found in molecular clouds. They form due to various dynamics, like shock waves or gravitational interactions (Arzoumanian et al. (2011)), and act as channels for material flow towards denser regions such as clumps or "cores." Cores are regions within clumps with even higher density and the

potential to gravitationally collapse and form proto-stars. In the early stages of star formation, proto-stars are surrounded by dusty and gaseous "envelopes" resulting from material interactions in their environment, obscuring them from visible wavelengths. These envelopes, extending from 300 to 3000 astronomical units (Pokhrel et al. (2018)), are crucial in nurturing and protecting proto-stars until they evolve into full-fledged stars.

The physical evolution of a new star can be described by different classes of Young Stellar Objects (YSO) Adams et al. (1987). These classifications depend on the slope of their infrared (and far-infrared) spectral energy distribution (SED) (Dauphas & Chaussidon (2011)). The slope of the spectral energy distribution is defined as α_{IR} and corresponds to the wavelength range between the near-infrared ($2\mu m$) and the mid-infrared ($25\mu m$) (Armitage (2017)). When α_{IR} is not defined, we refer to obscured sources (Class 0), with no emission in the optical or near-infrared range. When $\alpha_{IR} > 0.3$, there's an excess of infrared emission (Class I). When $-0.3 > \alpha_{IR} > 0.3$, we have Flat spectrum sources. When $-1.6 > \alpha_{IR} > -0.3$, we're dealing with Class II sources. Finally, when $-1.6 < \alpha_{IR}$, we refer to sources with at most a weak excess of infrared emission (Class III), this type of spectral energy distribution is similar to isolated stellar photospheres with classifications prior to the main sequence. This classification corresponds to a structural and evolutionary sequence that is divided into the following classes: Class 0 and Class I YSOs accumulate from discs, which, in turn, are being fed by gas falling from the envelopes; Class II YSOs, or classic T Tauri stars (for low mass stars) or Herbig Ae/Be stars (intermediate mass stars), are stars prior to the main sequence with surrounding disks; and finally, Class III YSOs are stars prior to the main sequence with little or no remaining primordial gas orbiting around them.

When the collapse in the core of the cloud begins, a protostar starts forming, which has a mass smaller than that of the core's envelope. The rotation of the core causes the material from the envelope to fall toward the young star, resulting in the formation of a disk around it. For the youngest YSOs (Class 0 and Class I), the disks are still being fed by the material falling from the outer layers of the envelope. On the other hand, the more evolved classes (Class II) have already shed their envelopes but retain massive gas disks, often actively accreting gas disks. When the gas disk dissipates completely, it leaves what is known as a Class III YSO.

From Figure 1.1, it is evident that Class I sources with envelopes are much less numerous compared to Class II YSO, or sources with disks but little or no envelope. Therefore, most of the circumstellar disk's lifetime consists of relatively isolated stellar disk systems that have completed the primary accretion phase from the envelope. From an observational standpoint, the primary focus is on isolated disks where envelope accumulation has nearly ceased; this corresponds to Class II YSOs and flat spectrum sources. Many current studies have demonstrated that these kinds of protoplanetary disks exhibit distinct structures in both dust and gas emissions.

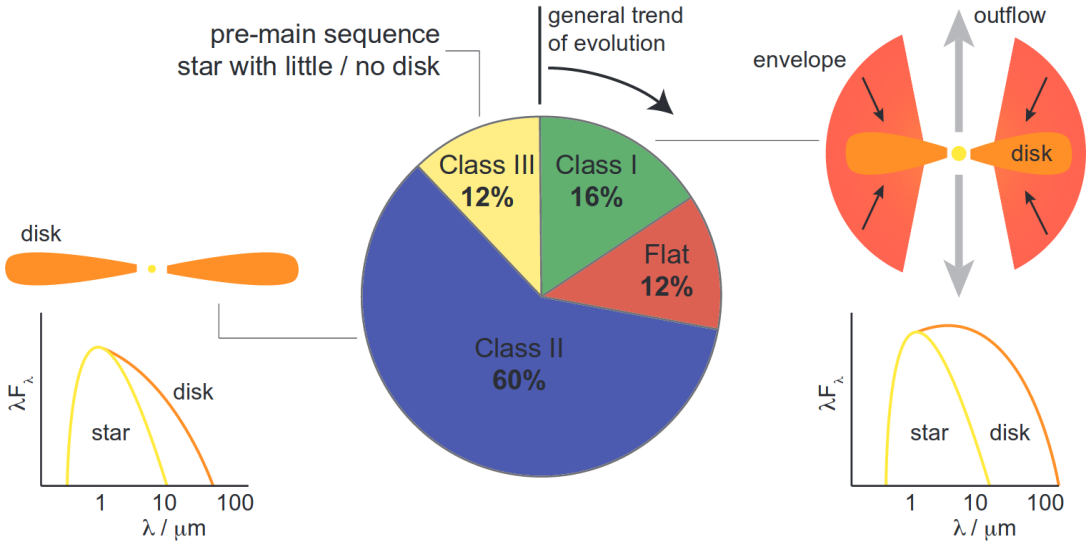

Figure 1.1: The figure shows the classification of Young Stellar Objects. The central image's diagram has been created based on data from the Spitzer c2d Legacy survey Evans et al. (2009), using the slope of the spectral energy distribution between the near-infrared and mid-infrared wavelengths. Figure from Armitage (2017)

In regions of low-mass star formation, they are usually the favorable sites where the formation of planets takes place. Planet formation is thought to take place in flattened disk-like structures that surround their host star. This is formed just after the birth of the star (protostar) and is enveloped by the protoplanetary disk. How and where these disks form is still a field of study, but what we do know is that protoplanetary disks generally reach sizes of about 100 au and show Keplerian rotation (Yen et al., 2013).

Protoplanetary disks were revealed by infrared and submillimeter observations, primarily on T Tauri stars (Rucinski, 1985); (Strom et al., 1989); (Adams et al., 1990). These detections took place thanks to the excesses of infrared radiation observed in the spectral energy distribution (SED). Infrared excess blackbody radiation from a star originates from thermal emission from dust around the young star. Through infrared observations, it has been possible to determine the basic properties of the disks, such as mass, density, size, and chemical composition (Williams & Cieza, 2011).

Millimeter observations also show the thermal emission of dust in the disks of class II sources. In addition to detecting rotational spectral lines (J levels) of small molecules such as CO and its isotopologues, where it appears that much of the disk is transparent at 1.3 mm, but the innermost regions less than 1au are not (Beckwith et al., 1990a).

The first detections of organic molecules in protoplanetary disks were made by submillimeter observations (Dutrey et al., 1997), in protoplanetary disks of DM Tau and GG Tau. Due to the low resolution with observations of a single dish, it is not possible to resolve the structure of the disk. However, through the use of interferometric techniques, it has been possible to resolve various structures in different sources (Andrews et al., 2018).

1.2 Protoplanetary Disk structure

The physical structure of protoplanetary disks often shows up as a kind of open fan if the cross-section of the disk around the star is taken. As illustrated in figure 1.2, the disk structure separates into layers that are dominated by gas density and temperature variations. The disk's rotation speed follows Keplerian rotation. The vertical structure is determined by a balance between gravitational forces and pressure gradients, resulting in varying density with height. Gas movement in the disk is influenced by mass accretion and turbulence driven by magnetorotational instability (MRI) ((Hartmann, 2001)(Shakura & Sunyaev, 1973)).

The temperature in the disk depends on the heating and cooling processes. Cooling is mainly due to thermal radiation from dust grains, while heating comes from the central star and turbulence. In the midplane, turbulent mixing dominates heating, resulting in a specific temperature distribution. Additional factors, like UV radiation from the interstellar medium and cosmic rays, also affect temperature variations in the disk.

As illustrated in the diagram, disks typically exhibit three distinct layers:

- The midplane: This region is the coldest part of the disk, where gas and dust share the same temperature, with dust cooling being the dominant process.

- The molecular layer: In this warm layer, the gas temperature exceeds that of the dust. The most abundant molecule is CO, and effective cooling mechanisms involve CO's ro-vibrational transitions and gas-dust collisions.

- The hot atmosphere: This layer reaches the highest temperatures and lower densities, where gas cooling is primarily influenced by Lyman-alpha emission and other atomic lines such as O$[I]$.

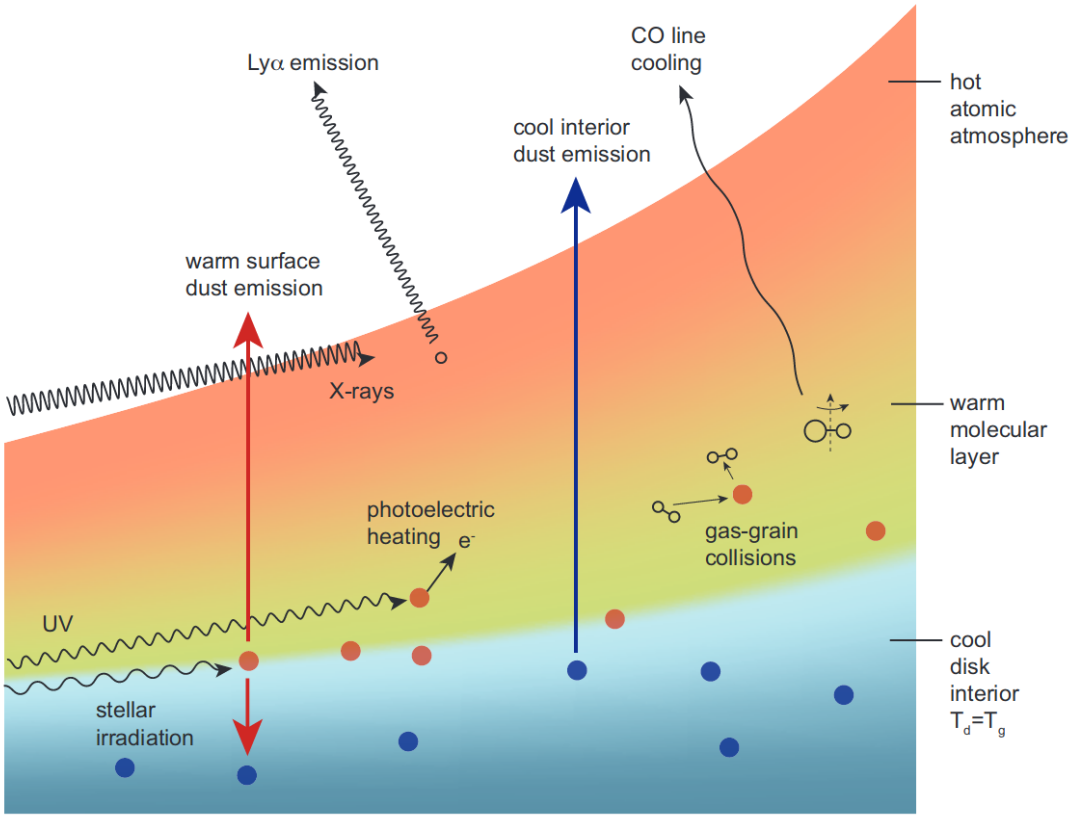

Figure 1.2: The figure shows the structure of the disk that results from these heating and cooling processes for each layer. Reference from Armitage (2017)

Chemical processes within the disks are significantly influenced by freeze-out and evaporation. When molecules in the gaseous phase adhere to the surface of a cold dust grain, an ice layer forms. When radiation from the host star reaches this ice mantle, the ice sublime, and the gas emits. This freezing process occurs when the dust grain's surface temperature drops below a critical value known as the evaporation temperature. This critical temperature varies for each molecule; for instance, for one of the most common molecules like CO, the temperature within the protostellar envelope is around 20 K. For H_2O, this temperature reaches 100 K Fraser et al. (2001). These temperatures can even differ based on whether the molecule is present in the hot regions ($T > 100$ K) or the cold envelope ($T < 100$ K) Bisschop et al. (2007).

When contemplating the rich chemistry occurring across different layers of the disk, it's crucial to also account for gas-phase recombination reactions. These recombinations involve molecular metal ions in the gas phase and recombination on the surfaces of dust grains. The gas-phase recombination can be illustrated by considering potential reactions between electrons and generic molecules, and metal atoms Oppenheimer & Dalgarno (1974). The fundamental reactions are:

- Ionization

$$m \rightarrow m^+ + e^- \ , \tag{1.1}$$

- Recombination with molecular ions

$$m^+ + e^- \rightarrow m \ , \tag{1.2}$$

- Recombination with gas-phase metal ions

$$M^+ + e^- \rightarrow M + h\nu \ , \tag{1.3}$$

- Charge exchange reactions

$$m^+ + M \rightarrow m + M^+ \ , \tag{1.4}$$

where m is a generic molecule and M metal atoms. Recombination on grain surfaces becomes more significant for smaller grain sizes.

1.3 Chemistry in Protoplanetary disks

Due to the challenges in accurately quantifying the total mass of material within disks using dust continuum data, a more effective strategy might involve molecular line emission. Protoplanetary disks house diverse chemical elements and molecules that originate from the molecular cloud from which the star and its circumstellar disk emerged. As matter accumulates within the disk, changing conditions facilitate the development of increasingly intricate molecules. Among these molecules could be organic compounds, hydrocarbons, and other precursors vital for forming planets and their atmospheres.

The formation of molecules and the detection of atomic lines within protoplanetary disks are pivotal aspects for comprehending the chemistry and evolution of these systems. These processes provide valuable insights into the composition of materials within the disks and the mechanisms involved in planetary formation. The process of molecule formation involves chemical reactions in the colder and denser layers of the disk, where the energy is low enough for atoms to combine and create molecules. Ultraviolet radiation from the young star can also play a role in both forming and breaking down molecules within different regions of the disk.

To investigate the chemical composition of protoplanetary disks, radio, and submillimeter observations are employed to detect emissions of atomic and molecular lines. Each molecule emits or absorbs radiation at specific low frequencies, enabling the identification of its presence and abundance within the disk. These molecular line emissions provide

insights into the temperature, density, pressure, and chemical composition of the gas in different regions of the disk. They also allow for tracking the material distribution, turbulence (Flaherty et al. (2015)), and studying the disk's dynamics (Teague et al. (2016), Flaherty et al. (2017)), including the presence of structures like rings, gaps, and spirals, which might actually indicate interactions between planets and the disk. Planets orbiting within the gas disk can create cavities and spirals, leading to local pressure maxima and vortexes that could trap dust in ring, arc, or horseshoe shapes.

Various non-thermal ionization sources are essential for enabling chemical processes within protoplanetary disks where stellar radiation cannot reach effectively. Ultraviolet photons, primarily from the central star or neighboring stars, play a key role in ionizing surface atoms, particularly at distances around 100 au. Stellar X-rays, emitted from the stars, contribute to ionization at larger scales but have limited penetration near the star due to higher densities. Cosmic rays are a potential source, particularly in denser molecular layers, but their presence depends on factors like stellar winds and magnetic fields. Radioactive decay also contributes to ionization, although it represents a relatively small fraction. Other less efficient sources, including spontaneous emission and energetic particle interactions, play minor roles. These non-thermal ionization sources collectively shape the chemistry and physical properties of protoplanetary disks.

Studies conducted in millimeter/submillimeter observations have highlighted molecules such as HCN and C_2H as particularly interesting to study because they are detectable in different rotational lines, show quite complex gas morphologies, and HCN has been detected in multiple protoplanetary disks, making it quite common. Some of the properties to consider about these molecules are:

HCN

- The radiation field of the young star permanently influences the abundant chemistry generated in the disks, especially UV radiation in the surface layer and in the molecular layer, which plays a significant role. In particular, emissions of HCN compared to CN (column density ratio of CN/HCN) have allowed the determination of how effective the dissociation of HCN is by UV photons ($\lambda > 113$ nm) from the host star Bergner et al. (2021a). Furthermore, this column density ratio increases with radius, meaning that HCN loses protection from dust in the outermost part of the disk, allowing for more effective photodissociation.

- It has been observed that HCN ices can behave in two ways. On one hand, the ice can directly sublimate, while on the other hand, it can become trapped. The latter scenario results in weaker emissions that may mix with other larger molecules in the ice, such as H_2O or CH_3OH. The presence of a planet in the disk would produce heating in the ice around it, allowing certain species like HCN to sublimate Cleeves

et al. (2015). This makes HCN a strong candidate as a tracer for planets forming in the midplane of the disk.

- HCN is one of the few nitrogen-bearing molecules detected in protoplanetary disks, so its detection allows us to understand the nitrogen reservoirs deep within the disks. The detection of isocyanides and cyanides is important as they are precursor molecules for prebiotic chemistry (Powner et al. (2009)).

- HCN and other nitrogen-bearing species are formed through the fractionation atomic N (and N_2 Heays et al. (2014)), via the following reaction:

$$N + CH_2 \longrightarrow HCN + H, \tag{1.5}$$

- The non-thermal desorption of molecular hydrogen, H_2, due to the heating of grains by cosmic rays, allows for a high concentration of small molecules like HCN in the gas phase (Hasegawa & Herbst (1993)).

$$CN + H_2 \longrightarrow HCN + H. \tag{1.6}$$

C_2H

- Observations in disks like TW Hya and DM Tau have shown that hydrocarbon emissions, such as C_2H, extend beyond the submillimeter dust emissions. However, the redistribution of dust shifts the UV opacity, leaving the disk surface and outer disk essentially dominated by UV photons. In the inner disk region, carbon may also be depleted due to the formation of refractory grains or its adherence to larger bodies that are less susceptible to evaporation, creating an inner hole for hydrocarbons Bergin et al. (2016a). Both effects could be ingredients for the formation of observed hydrocarbon rings (Kastner et al. (2015)).

- In Teague et al. (2018a), it has been observed that the minimum column density profiles of C_2H match very precisely with the locations of Jupiter-mass planets created in hydrodynamic simulations (at 83 and 137 au). The possibility that well-resolved column density profiles coincide with general gas density perturbations provides tracers for these planets located within those perturbations. C_2H is a good tracer because its hyperfine structure allows for a more effective determination of the column density profile (Bergner et al. (2019)).

- The formation pathways for C_2H are related to the overall C/O ratio in the disk, with the presence of atomic carbon (Bergin et al. (2016a)). The key formation pathways are:

$$C + H_3^+ \longrightarrow CH_3^+,$$

$$CH_3^+ + H_2 \longrightarrow CH_5^+,$$
$$CH_5^+ + H_2 \longrightarrow CH_3 + H_2,$$
$$CH_3 + C \longrightarrow C_2H_2,$$
$$C_2H_2 + h\nu \longrightarrow C_2H + H, \tag{1.7}$$
$$C_2H_2 + H_3^+ \longrightarrow C_2H_3^+ + H_2,$$
$$C_2H_3^+ + e^- \longrightarrow C_2H + H_2. \tag{1.8}$$

- Another possible pathway involves ionized atomic carbon reacting with molecular hydrogen. Now UV radiation is the key to initiating carbon ionization and generating free electrons for absorption (Bergner et al. (2019)), as shown below:

$$C + h\nu \longrightarrow C^+ + e^-,$$
$$C^+ + H_2 \longrightarrow CH_2^+,$$
$$CH_2^+ + e^- \longrightarrow CH + H,$$
$$CH + C^+ \longrightarrow C_2^+ + H,$$
$$C_2^+ + H_2 \longrightarrow C_2H^+ + H, \tag{1.9}$$
$$C_2H^+ + H_2 \longrightarrow C_2H_2^+ + H,$$
$$C_2H_2^+ + e^- \longrightarrow C_2H + H. \tag{1.10}$$

In summary, the formation of molecules and the detection of atomic and molecular lines within protoplanetary disks provide crucial insights into the chemical composition and dynamics of these systems during their formation. These studies aid us in comprehending the processes underlying planet formation and the evolution of planetary systems in their early stages.

1.3.1 Rotational Lines

Stars are gigantic factories of heavy elements that, in turn, form tiny solid particles: dust grains. Dust is ejected into the interstellar medium at the end of a star's life, and there, mixed with molecular gas, it acts as a screen that prevents us from seeing the new stars and planets forming within those clouds. Of the radiation emitted by the obscured objects (whether they are proto-stars, protoplanets, etc.), only mm/submm waves are capable of escaping the surrounding cloud. Therefore, it is only thanks to these radiations

that it is possible to observe these forming objects.

The radiation emitted by interstellar dust takes place in the same mm/submm domain, and the same applies to the molecules that make up the gas in interstellar clouds. The study of these radiations provides the only reliable means of diagnosing the physical conditions (such as density and temperature) and the chemical composition of the environment in which stars and planets form.

Spectral lines observed in the mm/submm range are primarily formed in the molecular gas of circumstellar and interstellar clouds. Transitions between the lowest rotational levels of a large number of molecules (i.e., photons emitted when a rotating molecule slows down its rotation) occur in the millimeter domain. A spectral line has a very specific wavelength, making it an unmistakable "signature" of the presence of the corresponding molecule. In the mm/submm domain, there are more than 1000 known spectral lines. This high number of spectral lines, along with the reasons mentioned earlier, makes the mm/submm range the most suitable for studying interstellar clouds, objects embedded within the clouds, and the entire cold universe.

Rotational transitions primarily occur between different rotational levels of the same vibrational state, although in light molecules, there are many examples of combination rotational-vibrational transitions. Incident electromagnetic waves, provided they have an electric dipole moment, can excite the rotational levels of molecules. The electromagnetic field exerts a torque on the molecule.

The rotational spectrum of a diatomic molecule consists of a series of evenly spaced absorption lines, typically in the microwave region of the electromagnetic spectrum. The energies of the spectral lines are $J(J+1)B$ for transitions $J \longrightarrow J+1$, where J is the quantum number of rotational angular momentum, and B is the rotational constant.

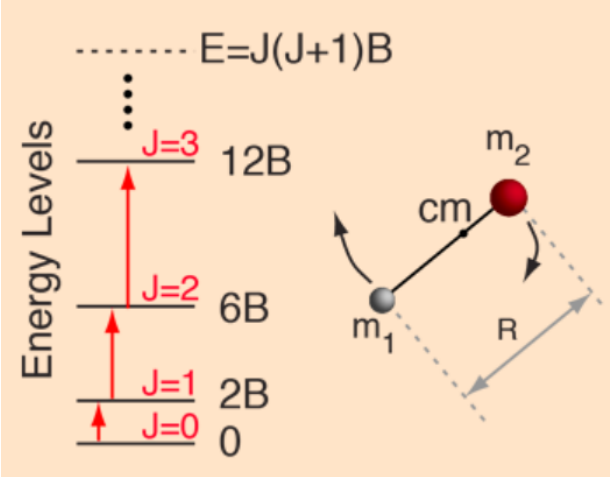

Figure 1.3: The figure shows the diagram of rotational transitions according to their rotational energy level, where E corresponds to the energy of the level ($h\nu$), J is the quantum number of rotational angular momentum, B is the rotational constant, and R is the bond length. Image reference from http://hyperphysics.phy-astr.gsu.edu.

1.4 DSHARP Project

Observations show that a significant portion of the physical processes that govern the formation of planets, stars, and galaxies, as well as the early evolution of all these objects, occur in a very low-temperature material (typically 10-100 K). This "cold universe" emits hardly any optical radiation (or higher-frequency radiation), meaning it is not observable with conventional telescopes. However, this cold matter does emit radiation in radio waves, preferably in the millimeter and submillimeter (mm/submm) ranges of the spectrum.

Protoplanetary disks are generally dominated by the contribution of ice grains and rocks. To determine some parameters such as the temperature and the mass of the disks, in addition to the size of the dust particles, the observation is made using dust emission or continuum radiation (Andrews et al. (2009)). When observing dust within disks around nearby young stars, spatially resolved data can offer more direct insights into a wide spectrum of potential density structures. Measurements at millimeter wavelengths are particularly advantageous, as the thermal continuous emission from dust grains remains optically thin, thus allowing for a comprehensive exploration of the entire disk volume (Beckwith et al. (1990b)).

Observing these substructures within disks presents a significant challenge due to the requirement for high spatial and spectral resolutions to detect them. Nonetheless, through high-resolution observations, it has been unveiled that these variations in material distri-

bution exhibit intricate substructures, such as azimuthal or geometric asymmetries and spiral arms, which are quite common. Additionally, it's believed that disks often display complex structures like rings and gaps. These substructures are likely pivotal factors in numerous disk evolution processes and, consequently, in planet formation. Detecting these bright signatures generated by millimeter/centimeter-sized particles can be achieved using submillimeter continuum observations. Depending on the resolution, it becomes possible to determine the scales, locations, and amplitudes of these disk substructures.

Should these substructures have been prominent during the initial phases of disk evolution, it's plausible that the creation of planetesimals and even complete planetary systems could have occurred much more efficiently than predicted by conventional models.

DSHARP (Disk Substructures at High Angular Resolution Project) is a collaborative effort that harnesses the unique capabilities of ALMA to observe protoplanetary disks at millimeter and submillimeter wavelengths. It stands as one of the most extensive initiatives focused on characterizing substructures in the spatial distribution of solid particles. Its primary objective was to observe the continuous emission of 20 nearby, bright, and large protoplanetary disks at extremely high resolution ($\sim$0.035 arc-seconds) in continuum at a frequency of 240 GHz and ^{12}CO line emission (J transition 2 to 1). These wavelengths are particularly suitable for studying the dust and gas within disks, as they can penetrate dense regions and allow to peer through the surrounding interstellar material around young stars.

The DSHARP unveiled, for the first time, that these substructures are present throughout the sample as you can see in Figure 1.4. These substructures become clear only when the continuum emission has a resolution of a few astronomical units. They manifest as bright, narrow, concentric rings, and dark gaps. However, some disks exhibit large-scale spiral patterns (3 sources) and azimuthal asymmetries, including substructures potentially resonating with the mid-plane motion and "double gap" features, which could hypothetically suggest the presence of planets (Huang et al. (2018)). These substructures tend to be compact, ranging from 5 to 150 au, and their brightness varies across different sources.

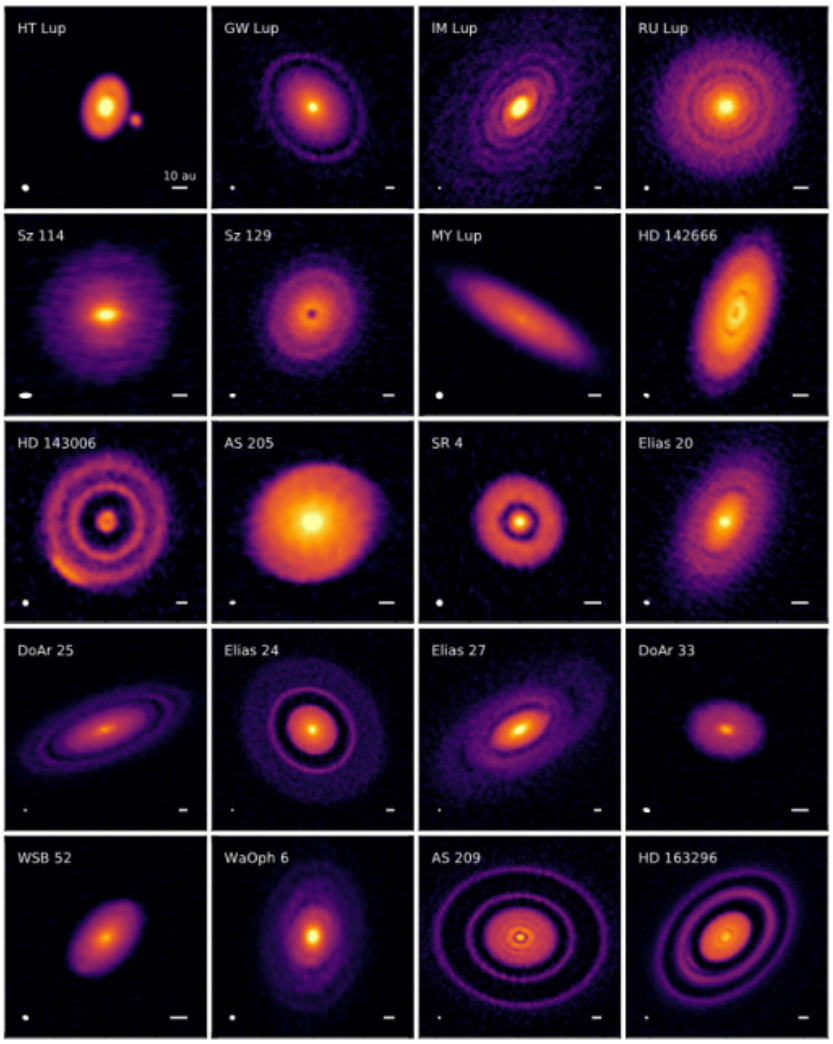

Figure 1.4: The figure shows the gallery of the 20 protoplanetary disks from the DSHARP sample. The image shows continuous emission at a frequency of 240 GHz (1.25 mm). Dust substructures are present in each of the sources. These emissions are in scale ranges from 5 au to more than 150 au. For more detail on the dimensions and intensity scales for each source see Kurtovic et al. (2018) and Huang et al. (2018). Reference from Andrews et al. (2018).

One of the most intriguing details unveiled by the DSHARP project, pertinent to the current investigation, involves the asymmetries observed in the continuous dust emission within the HD 163296 disk. At small scales, new structures like dark gaps (∼10 au) and a bright ring (∼15 au) have emerged. At larger scales beyond 50 au, two new bright rings have been identified, centered at 67 and 101 au. Additionally, a pair of dust crescents centered between 4 and 55 au and several weaker azimuthal asymmetries have been observed Isella et al. (2018) and Garrido-Deutelmoser et al. (2023). These asymmetries observed further support the hypothesis that the intricate structure of the HD 163296 disk is

a consequence of gravitational interaction with yet-to-be-detected planets (see Figure 1.5).

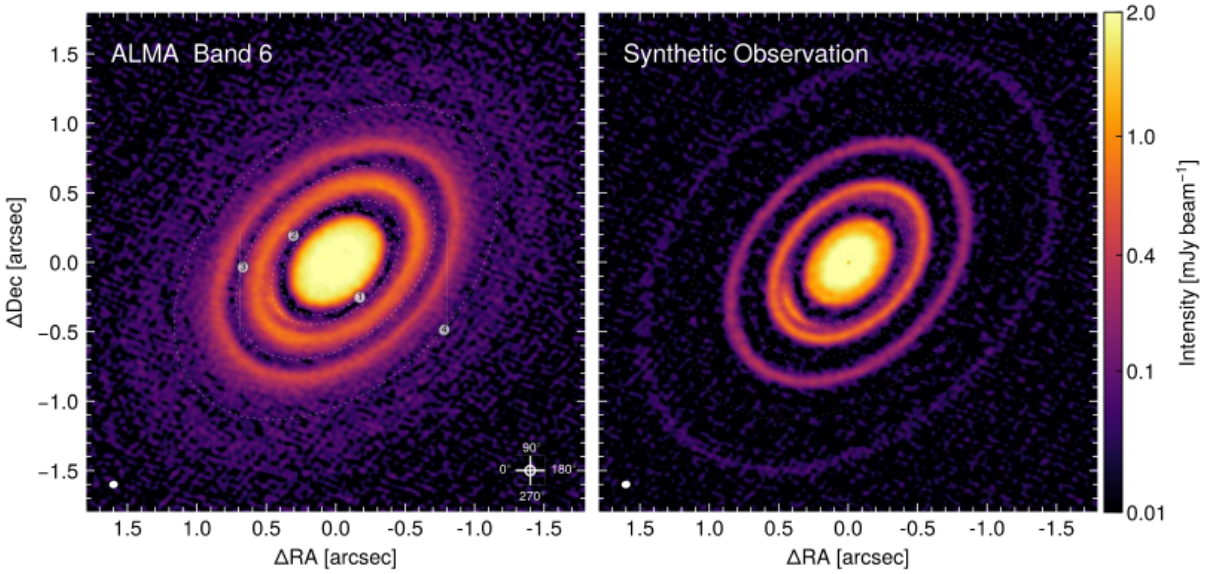

Figure 1.5: From Garrido-Deutelmoser et al. (2023), the presence of two planets with mass smaller than Saturn in the gap at ∼48 au, where the characteristic crescent observed in the HD 163296 disk (54 au) is located, has been modeled. In the figure: the left panel shows the dust continuum image for the HD 163296 disk taken with ALMA (Isella et al. (2018)). The numbered white dots indicate the positions of four potential planets, and the dashed lines represent their orbits in the simulation. The right panel corresponds to the image of the synthetic model.

1.5 Science target: The HD 163296 protoplanetary disk

The Herbig Ae/Be stars (HAeBes) cover a crucial mass range that links low-mass stars ($< 2M_{\odot}$) and high-mass stars (2-10 $M_{\odot}$), making them an ideal window for exploring their formation and evolution (Fairlamb et al. (2015)). The HD 163296 star system, at its center, hosts a young Herbig Ae star, with spectral type A1, an age of approximately ∼6 million years, and a mass of nearly ∼2 solar masses. HD 163296 is located in the Sagittarius constellation and is at a distance of ∼101 parsecs from Earth (Wichittanakom et al. (2020)). The disk surrounding the star extends to about 550 au from the central star for a gas structure twice that of dust de Gregorio-Monsalvo et al. (2013).

Observations in the continuum and of CO isotopologues (^{12}CO, ^{13}CO, and ^{18}CO) have detected the presence of three circular dust-depleted gaps with radii of 60, 100, and 160 astronomical units (au). The morphology of the latter two gaps is consistent with gravitational perturbations caused by two giant planets orbiting at approximately 100 and 160

au (Isella et al. (2016)). With such large orbital radii and the young age of this disk, it implies that giant planets could form much farther from the central star and much more rapidly.

The Large Program DSHARP conducted high-resolution spatial observations of both the dust continuum emission and rotational emission lines of ^{12}CO ($J = 2 - 1$). These observations allowed for the characterization and resolution of the previously discovered bright dust rings in HD 163296 at radii of 68 and 101 astronomical units (au). Furthermore, the high spatial resolution led to the discovery of new substructures at small scales (10, 15, and 55 au) Isella et al. (2018). The observations of dust and CO emissions yield insights into the disk's vertical arrangement and enable a precise assessment of dust extinction's optical depth within the dust rings. Moreover, the observed anomalies in the dust continuum emission substantiate the theory that the complex structure of the HD 163296 disk arises from gravitational interactions with yet-to-be-detected planets. On the other hand, the location of giant planets in the outer regions of the disks would be consistent with gravitational instability. Through the comparison of 3D models of hydrodynamic and radiative transfer of giant planets, it is suggested that the observed deviation from Keplerian flow around HD 163296 is consistent with the kinematic signature of a planet embedded in the midplane of the disk. This planet would have twice the mass of Jupiter and would be located at a distance of approximately 260 au from the central star (Pinte et al. (2018)).

Just like dust, gas, and molecular lines are also key sources of information about the physical and chemical processes associated with planet formation in protoplanetary disks. Often, gas tends to have a larger extent than dust. Observations using ALMA in Band 6 have revealed that the emission of molecular lines such as HCN and C_2H often extends beyond the dust disk, even displaying substructures with a variety of morphologies such as arcs, wide gaps or bright rings in disks like DM Tau, V4046 Sgr, and HD 163296 Bergner et al. (2019).

The chemical composition of newly forming planets within a disk depends mainly on the material distribution in the regions closest to the star (<100 au). More recent observations using molecular lines at unprecedented spatial scales (ALMA large program, **MAPS**[1] Öberg et al. (2021a)) have shown that the distribution of small organic molecules like HCN and C_2H would have a decrease in their column density within dust gaps. This could be in agreement with both the dust and gas distribution being affected by the presence of a planet located in these dark gaps (Guzmán et al. (2021a)). HCN has been proposed as one of the best tracers of giant planets in disks since the planet's heating effects would result in increased HCN emission (Cleeves et al. (2015)). Furthermore, HCN and C_2H would be visible in different rotational lines, allowing for additional information to be determined, such as the temperature of the environment around the planet.

[1]**Molecules with ALMA at Planet Formation Scales**

HD 163296 also exhibits a relatively large fraction of similar lines. This is because the emission structures are consistent within the sample in each disk in **MAPS**. For instance, HD 163296 shows multiple co-spatial rings of comparable widths in different molecular lines. CO isotopologues are the most consistent with each other, which is not surprising, considering that all lines originate from the same species. Species belonging to the same molecular families, for example, C_2H and c-C_3H_2; HCN and HC_3N, as well as different transitions of a single species, for instance, HCN 3–2, 1–0; C_2H 3–2, 1–0, are also often similar to each other (Law et al. (2021a)). This is an intuitive result as radial profiles appear similar, with consistent multi-ring emission structures, for example, C_2H and c-C_3H_2 in HD 163296. The correlation patterns appear quite complex, as for some lines, they are consistently well correlated, while for others, they are not. For example, the relationship between HCN and H_2CO is very different in HD 163296, as is the case for the C_2H and CO lines.

HD 163296 is a very well-studied disk, not only in infrared and submillimeter observations of dust and gas but also in exploring more complex chemistry. Results published in Ilee et al. (2021), from **MAPS** large program, indicate that disks like HD 163296 are important reservoirs of complex organic molecules (COMs), such as HC_3N, CH_3CN, and c-C_3H_2. The emission of these kinds of molecules is compact and extends in the same way as dust, suggesting that frozen dust might be related to the formation of these complex molecules.

1.6 Motivation

The main goal of this research is to map the chemistry of small organic molecules in the HD 163296 protoplanetary disk. To achieve this, observations made by the ALMA Large Program, **MAPS**, will be used. These observations at different spatial scales, Band 3 at 0.5", corresponding to radial scales between 20-50 au, and Band 6 at 0.2", corresponding to radial scales of 10-20 au, will provide unprecedented details in the regions where planetesimal structures are forming, including spectral information about the distribution of organic molecules.

The distinctive morphology exhibited by the HD 163296 disk, both in the continuum and in the millimeter-wave gas, makes it an exceptional candidate for study. Due to its size and the distance at which HD 163296 is located, it has been possible to resolve the distribution of molecular gas, specifically small organic molecules through their rotational transition lines, particularly HCN and C_2H. These small molecules are particularly interesting due to their prebiotic properties, organic ice chemistry, their relationship to cyanides and hydrocarbons, and fundamental C/N ratios.

Parameterizing the gas substructures exhibited in HD 163296 allows for a better understanding of the regions where richer chemistry takes place in the early stages of high-mass protoplanetary disks. It also enables the quantification of physical structures, such as gap sizes, their abundance, emission height, and their relationship with millimeter and submillimeter dust.

Chapter 2

Observations

2.1 MAPS project

The Molecules with ALMA at Planet Formation Scales (MAPS) project aims to expand our understanding of the chemistry in the environment where planet formation occurs. Its goal is to explore protoplanetary disks by observing them with unprecedented angular resolution, allowing the resolution of structures down to scales of 10 au. These disks were observed in four spectral configurations, collectively covering approximately 50 lines from more than 20 different molecular species. The MAPS sample consists of five sets of disks selected based on their stellar properties, structures, substructures, and their capacity for molecular line detections. The sample includes both T Tauri and Herbig Ae stars, which exhibit different types of dust substructures and may be related to chemical substructures, with ongoing planet formation potentially occurring. These disks were resolved using ALMA with continuous observations at 0.1", and they were included in observation programs related to disk chemistry (Dutrey et al., 2007); (Öberg et al., 2010); (Öberg et al., 2011); (Huang et al., 2017); (Bergner et al., 2018). From the ALMA Large DSHARP program (Andrews et al., 2018), five disks around different types of young stars were selected, based on the diversity of their dust substructures.

A wide diversity of radial morphologies has been observed, including rings, gaps, and plateaus, both within each disk and across the entire MAPS sample Öberg et al. (2021a). This diversity in line emission profiles is also present in the innermost as well as the outer regions. Overall, this suggests that planets form in chemically varied environments, both among disks and at different radii within the same disk. However, some chemical substructures in the inner disk and most of the outer chemical substructures (>150 au) cannot be directly linked to dust substructure, indicating that other causes of chemical substructures also exist, such as snowlines, gradients in ultraviolet photon fluxes, ionization, and radially varying elemental ratios. This implies that chemical substructures could become powerful probes of different disk characteristics (Law et al. (2021a)), in addition to influencing the environments in which planets form.

The goals of the MAPS project are to explore the chemistry at unprecedented spatial resolutions within protoplanetary disks. The sample of the selected five disks has revealed a great diversity of dust substructures, and one of the main objectives is to identify the links between the dust and the chemical substructures. None of the disks in the sample is substantially obscured by cloud material, nor do they appear to include emissions from substantial envelopes that would affect the interpretation of molecular line observations. All disks have been previously observed in at least a subset of the target molecular lines, allowing for constraining the emission heights of the observed molecules and assessing how well the planet-forming layers could be explored. The high spatial resolutions achieved in the MAPS project enable the investigation of C/N/O/S ratios, deuterium fractionation, and organic compositions on scales of 10 au. This allows the study of chemistry in the deeper regions of the disks, where planetary formation takes place. Furthermore, the sample includes both T Tauri and Herbig Ae stars, which will allow for exploring the importance of stellar luminosity and magnetic fields in shaping the chemistry around this kind of star.

The new high-resolution observations of multiple molecular lines conducted by the MAPS large program have unveiled various gas structures in different types of protoplanetary disks. These substructures are fascinating to study because they could be related to the presence of embedded planets within the disks.

2.1.1 Line targets

The MAPS project observed five disks in four spectral setups, two for Band 3 and 2 for Band 6. The project selected lines that had been previously detected in disks. For Band 6, all lines targeted were detected in at least some of the disks in the MAPS sample. Otherwise, for band 3, most of the lines targeted had not been previously observed in any disks in the sample. This spectral lines setup incorporates CO molecules (isotopologues) that tracer mass, kinematics, and gas structure. Also tracers of O/S and C/N ratios (C_2H, HCN, CO isotopologues, and CS), disk organic inventories, and chemistry (C_2H, HCN, H_2CO, c-C_3H_2, HC_3N, CH_3CN), photochemistry (CN and C_2H), deuterium fractionation (DCN and N_2D+) and disk ionization (HCO^+, $H^{13}CO^+$, and N_2D^+). Furthermore, for HCN, CN, $C^{17}O$, and C_2H lines had been resolved its hyperfine structure, which is used to determine the line excitation conditions for example temperature, density, line optical depth, and column densities. For ^{13}CO, $C^{18}O$, HCN, C_2H, HC_3N, and CH_3CN were observed in bands 1 mm and 3 mm, band 6 and band 3 respectively.

In particular, in this research, we focus on two specific molecular lines, HCN and C_2H. These molecules have been observed in protoplanetary disks previously, and exhibit rather distinctive characteristics when observed, and therefore, they are highly interesting study targets. See table 2.1 for more details about the setups for HD 163296.

Species	QN	ν (GHz)	$log_{10}(A_{ij}/s^{-1})$	g_u	E_u (K)
		Setup B3-1			
HCN	J=1-0, F=1-1	88.630416	-4.6184	3	4.3
	J=1-0, F=2-0	88.631848	-4.6185	5	4.3
	J=1-0, F=0-1	88.633936	-4.6184	1	4.3
C_2H	J=3/2-1/2, F=2-1	87.316898	-5.6560	5	4.2
	J=3/2-1/2, F=1-0	87.328585	-5.7367	3	4.2
		Setup B6-2			
HCN	J=3-2, F=3-2	265.886434	-3.1292	7.0	25.5
	J=3-2, F=3-3	265.884891	-4.0322	7.0	25.5
	J=3-2, F=2-2	265.888522	-3.8861	5.0	25.5
C_2H	J=7/2-5/2, F=4-3	262.004260	-4.1152	9	25.2
	J=7/2-5/2, F=3-2	262.006482	-4.1321	7	25.2
	J=5/2-3/2, F=3-2	262.064986	-4.1521	7	25.2
	J=5/2-3/2, F=2-1	262.067469	-4.1906	5	25.2
	J=5/2-3/2, F=2-2	262.078935	-5.0619	5	25.2

Tabla 2.1: Spectral set-up 1 using band 3, and set-up 2 using band 6 in ALMA large program observation MAPS (at 3 mm and 1mm, respectively). The table shows the spectral window targets for HCN and C_2H species. Columns 2, 3, 4, 5, and 6 are Quantum numbers, rest frequency, base 10 logarithm of the integrated intensity, upper state degeneracy, and upper state energy, respectively. For more details and other species, refer to Öberg et al. (2021b).

2.1.2 Observational details

The MAPS project was executed between October 2018 and September 2019, and divided into 2 main executions, long and short baseline executions. The short-baseline executions were observed between October 2018 and April 2019, and the long-baseline executions in August and September 2019, with a total of 80 executions. Most of these executions consisted of 45 min on target and 20-45 min of calibrations (with longer calibration for longer baseline observations). HD 163296 was observed using from 43 to 49 antennas, in band 3, and band 6 used 43 to 47 antennas, with baselines from 15 to 3.638 meters for both bands. One of the main characteristics of MAPS configuration was the two observing modes in the correlator, two set-ups for each band (B3-1, B3-2, and B6-1, B6-2). Each setup consists of 6-9 spectral windows, one for a continuum band with a coarse velocity resolution of 1.4-3.4 km/s. The other spectral windows were designed to have a velocity resolution of 0.19-0.49 km/s for B3-1 and B3-2, and 0.09-0.20 km/s for B6-1 and B6-2 (for more observational details see the table 2.2).

2.2 Data reduction

2.2.1 Data Calibration

The ALMA calibration pipeline was initially the first step for all data calibration by ALMA staff. The long and short baseline data were calibrated separately because there not observed completely at the same time, therefore, not all data were calibrated using the same pipeline version. Different versions of CASA software were used from 2018 to 2019 (CASA 5.4 and CASA 5.6). Self-calibration step was also necessary, creating pseudo-continuum visibilities by flagging the line emission in each spectral window. For HD 163296 and CO 2-1 lines, were flagged channels with a range bigger than the other lines, because it includes extended emission, the disk winds (Klaassen et al., 2013). The spectral windows have a range of systemic velocities between 4.5 and 5.8 km/s, HD 163296 CO 2-1 line case of -10 and 20 km/s. Second, the pseudo-continuous data was averaged over 125 MHz channels and images were taken of each execution block. The continuum peak emission was identified and used to align the different executions to a common phase center. The self-calibration process starts with short-baseline data and is then concatenated with the long-baseline data, and the combined visibilities were self-calibrated together. To improve the signal-to-noise ratio (SNR) it was combined SPWs and scans were in the self-calibration of the Band 3 short-baseline data and in the self-calibration of the combined data of both settings (not necessary for Band 6 short-baseline data due to its higher continuum brightness). Tclean task was used to get an image after the self-calibration process, using a Briggs robust parameter of 0.5 and an elliptical mask. The mask dimensions and position angle were selected based on the inclination and position angle of each disk. The data

Setting	Date	# Ant.	Int time. [min]	Baseline [m]
B3-1	2018-10-22	48	36	15–1398
	2019-08-23	43	37	41–3144
	2019-08-24	45	37	41–3396
	2019-08-25	45	37	41–3396
	2019-09-04	46	37	38–3144
	2019-09-05	49	37	38–3638
B3-2	2018-10-25	49	36	15–1398
	2019-08-19	47	37	41–3638
	2019-08-22	46	37	41–3638
	2019-09-06	46	37	41–3638
B6-1	2018-12-04	43	41	15–784
	2019-08-16	45	43	41–3638
	2019-08-16	47	43	41–3638
	2019-08-17	47	43	41–3638
B6-2	2019-04-07	43	35	15–500
	2019-08-21	44	47	41–3638
	2019-08-25	45	47	41–3638
	2019-08-26	45	47	41–3638

Tabla 2.2: The table shows all ALMA executions for the source HD 163296 in the MAPS project. Include observational details such as set-up mode, observing date, number of antennas, on source integration times and baselines. For details such as spatial resolution, maximum recoverable scale, and phase and flux calibrators see Öberg et al. (2021b)

.

products are publicly available for download from the ALMA Archive[1][2].

2.2.2 Data Imaging

In this subsection, we will focus on the theory of interferometric image reconstruction based on the CLEAN algorithm. We will address the image reconstruction process in a standard manner, using the **tclean**[3] task from the CASA software, and define its main parameters.

The CLEAN algorithm is a fundamental technique in the processing of interferometric image data. It was developed in the 1970s and is widely used for cleaning interferometric images, especially in observatories like the Very Large Array (VLA) and the Atacama Large Millimeter/Submillimeter Array (ALMA). The reconstruction of radio interferometric images is formed from the visibilities obtained after the calibration processes. The main function of the CLEAN algorithm is to remove interference sources and improve the quality of astronomical images obtained from interferometric data. The **tclean** algorithm is a task that handles both continuum images and spectral line cubes. It contains standard cleaning-based algorithms along with algorithms for wide-band and multi-scale image reconstruction.

Interferometric images often exhibit undesired features such as side-lobe effects (due to the antenna's diffraction pattern) and artifacts stemming from the incomplete structure of the measured Fourier information. The CLEAN algorithm is based on the concept that astronomical sources can be viewed as a series of bright points in the image. The idea is to identify and remove these points one by one, progressively restoring the original image.

The algorithm operates by first identifying the location of the brightest source in the interferometric image. This is done by searching for a pixel with the highest value. Subsequently, a model of the identified source is created and subtracted from the original image. This leaves a residual that contains information about the remaining sources and side-lobe effects. To prevent significant side-lobe effects in the residual, a "Cleaning" process is applied to the residual image. This involves smoothing the residual image before the next iteration of the algorithm. Finally, the above steps are repeated iteratively until enough sources have been identified and removed, or until a predefined convergence criterion is reached. Once the sources of interest have been identified and removed, the model of the restored sources is added back to the whitened residual image to obtain the final restored image. This image should be cleaner and free from side-lobe effects compared to the original raw image.

[1] https://almascience.org/alma-data/lp/maps
[2] https://alma-maps.info/
[3] https://casa.nrao.edu/docs/taskref/tclean-task.html

The CLEAN algorithm includes several control parameters that can be adjusted according to the specific characteristics of the data used. Some of the arguments of the tclean algorithm used are defined below:

- **vis:** The abbreviation for "visibility". It corresponds to the processed data ready for reconstruction. Generally, the file has an extension ".ms" (Measurement Set).

- **imsize:** referring to the size of the image or the number of pixels.

- **cell:** pixel size in the image. As a general rule, it can be obtained by dividing the resolution of the interferometer in a specific band by five or eight.

- **weighting:** regarding the weighting of visibilities according to the UV-plane. For short baselines, the *Natural* value is recommended, also improving surface brightness sensitivity. For the opposite case, the parameter *Uniform* is established, obtaining better spatial resolution, and weighting long baselines. Finally, it could be said that an intermediate weighting of the baselines is established by the *Briggs* parameter.

- **robust:** Robustness parameter for Briggs weighting. It is more appropriate for detection experiments where sensitivity is more important. Provides weighting in sensitivities for long and short baselines.

- **specmode:** interpreted as spectral mode. It is established according to the scientific requirement, that is, if it is necessary to study continuous emission, this parameter is established as *'cont'*. For line studies, it is defined as *'cube'*.

- **restfreq:** rest frequency value to use for the image to be reconstructed.

- **nchan:** is established in studies of spectral lines. The parameter corresponds to the number of channels in a data cube. If there is no certainty in the exact channels where the line should be, it is recommended to leave said parameter free.

- **start, width:** velocity of the channel where cleaning begins and the width of the channel, respectively. Both values in units of speed (km/s).

- **niter:** referring to the number of iterations before the end of the major cleaning cycle. Numbers in the order of a thousand are recommended, avoiding closing the interactive window of the task, earlier than desired. To generate a dirty image, it is set equal to zero.

- **threshold:** Stopping threshold (number in units of mJy). A global stopping threshold that the peak residual (within clean mask) across all image planes is compared to.

- **interactive:** It refers to an interactive loop. In general, it is recommended to define masks containing real emissions interactively. It is possible to create regions without seeing the initial model through limit parameters. For dirty image builds is recommended to set this parameter to False, in addition to *niter* equal to zero.

- **imagename:** The name of the image to be reconstructed. However, it is recommended to choose a name that is relevant to the source of interest. Additionally, this command generates five other images as reconstruction products.

For more details about the outlines of the parameters defined above (and other parameters not used in this investigation), the CASA software documentation can be consulted https://casa.nrao.edu/docs/taskref/tclean-task.html and https://casa.nrao.edu/casadocs/casa-6.1.0/global-task-list/task_tclean/about.

After providing the input parameters and running the "tclean" task, the main product delivered is a reconstructed image using the CLEAN algorithm. Additionally, six other output images are generated, like cleaning image (**.image**) and residual image (**.residual**) (from tcleal algorithm); Moment-zero image (**.mom0**) (from immoments task); etc. For more details about the images generated after cleaning, consult the appendix B.

2.3 Data visualization

In this section, the results of image reconstruction for the protoplanetary disk HD 163296 will be presented. The images correspond to the data cubes for bands 3 and 6 (3 and 1 mm, respectively), as well as the moment 0 maps for each band. The creation of both types of images is a consequence of the techniques explained in the previous section using the **tclean** algorithm.

The first step is to create a conservative image with "tclean" task in order to determine the stopping criterion for iterations and to visualize if the channels match their respective velocities. Once these parameters are obtained, we proceed to run the "tclean" task again, and an interactive window will appear where you must select the areas where there is real source emission (see figure 2.1)). These regions can be selected using different types of masks; in this case, elliptical masks were chosen. This process is repeated until the residual becomes comparable to the background emission in the reconstructed image.

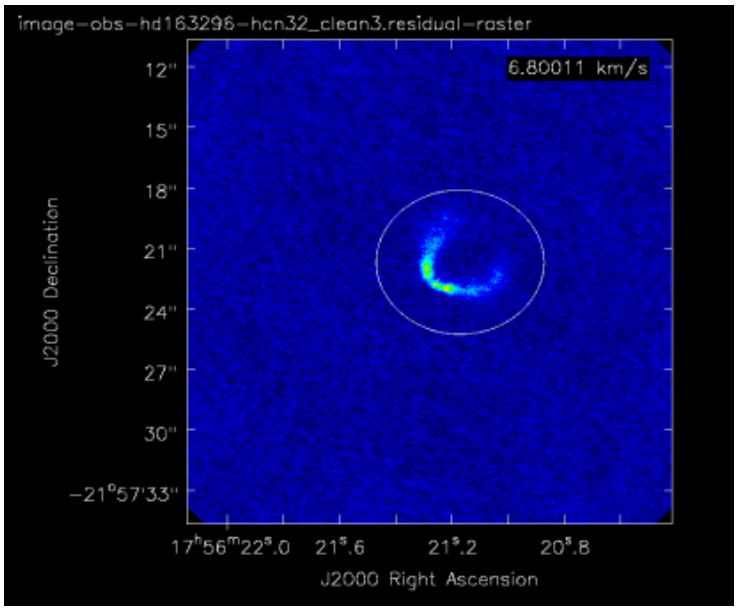

Figure 2.1: The figure shows the interactive interface of the CASA software, where an elliptical mask has been selected around the broadcast of the HD 163290 disk.

The data cleaning process with the tclean tool in the observations of HD 163296 for the HCN and C_2H molecular lines in bands 3 and 6 involves configuring various parameters. These parameters are adjusted specifically to achieve accurate and meaningful results in the study of this astronomical source.

The reconstruction of a data cube includes information about the spatial and spectral distribution of molecular lines in different channels. Additionally, we define the number of channels in the data cube, the channel width, and where each channel starts. These values are adjusted according to the characteristics of the observations in each band and molecule and have been detailed in the following table 2.3.

Species	Rot/trans	nchan	width (km/s)	start (km/s)
Setup B3-1				
HCN	1-0	32	0.53	-5.2
C_2H	1-0	50	0.53	-71.1
Setup B6-2				
HCN	3-2	60	0.22	-0.9
C_2H	3-2	60	0.22	-27.8

Tabla 2.3: Spectral setup 1 using band 3, and setup 2 using band 6 in ALMA large program, MAPS. The table shows the spectral window targets for HCN and C_2H species. Columns 2, 3, and 4 are number of channels, channel width, and first channel speed.

The figures below contain the products after the cleaning process on the interferometric data taken by the MAPS project. You can visualize the zero-moment figures, 2.2 and 2.3). In addition, the figure (2.4, 2.5, and 2.6) shows the Kleperian rotation which is a consequence of the Keplerian velocities of the rotating gas in the neighborhood of the HD 163296 star. The channel maps of molecular lines of HCN and C_2H show the hyperfine structure in the rotational transitions J=3-2.

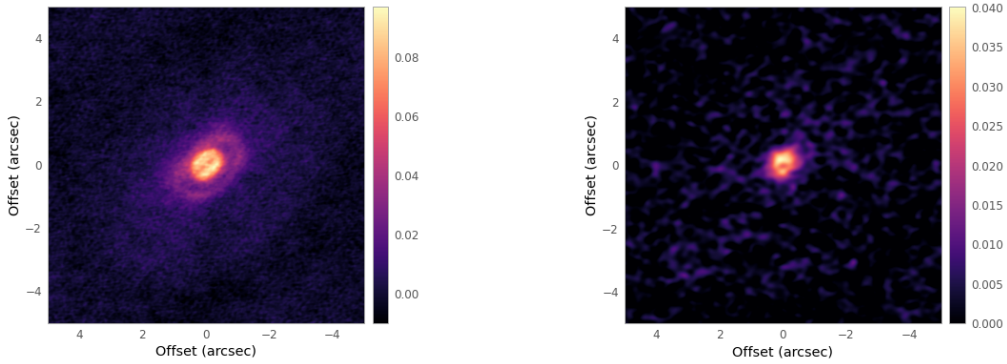

Figure 2.2: The figure shows the Moment-zero for the HCN line, on the left for band 6 (J=3-2) and on the right for band 3 (J=1-0) transitions. The intensity values in the color bar have units of mJk/beam.

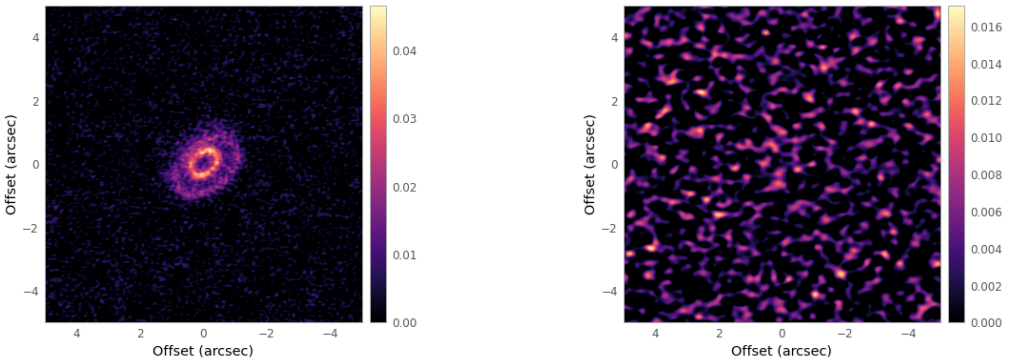

Figure 2.3: The figure shows the Moment-zero for the C_2H line for band 6 (J=3-2) and band 3 (J=1-0) transitions. The intensity values in the color bar have units of mJk/beam.

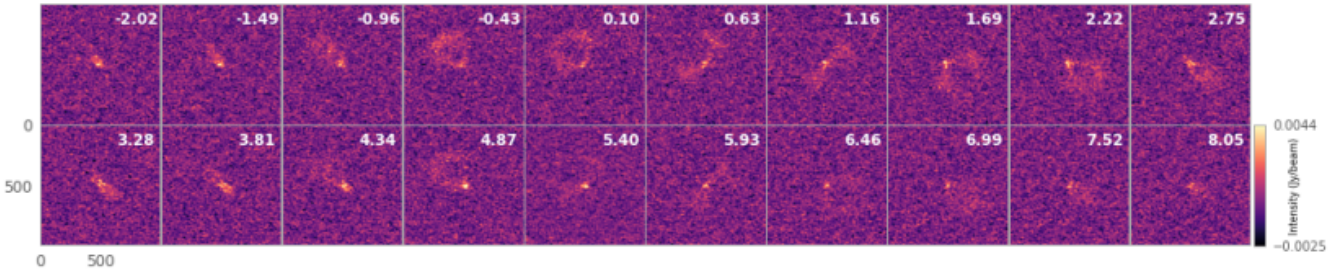

Figure 2.4: The figure shows the Channel map for the HCN line for band 3 (J=1-0) and includes a color bar of the intensity flux. For this figure, the minimum and maximum intensity values are -2.5 and 4.4 mJk/beam respectively.

For the C_2H molecule in band 3, it was not necessary to put the velocity map since the detection is imperceptible, and the figure only showed noise as you can see in Figure 2.3.

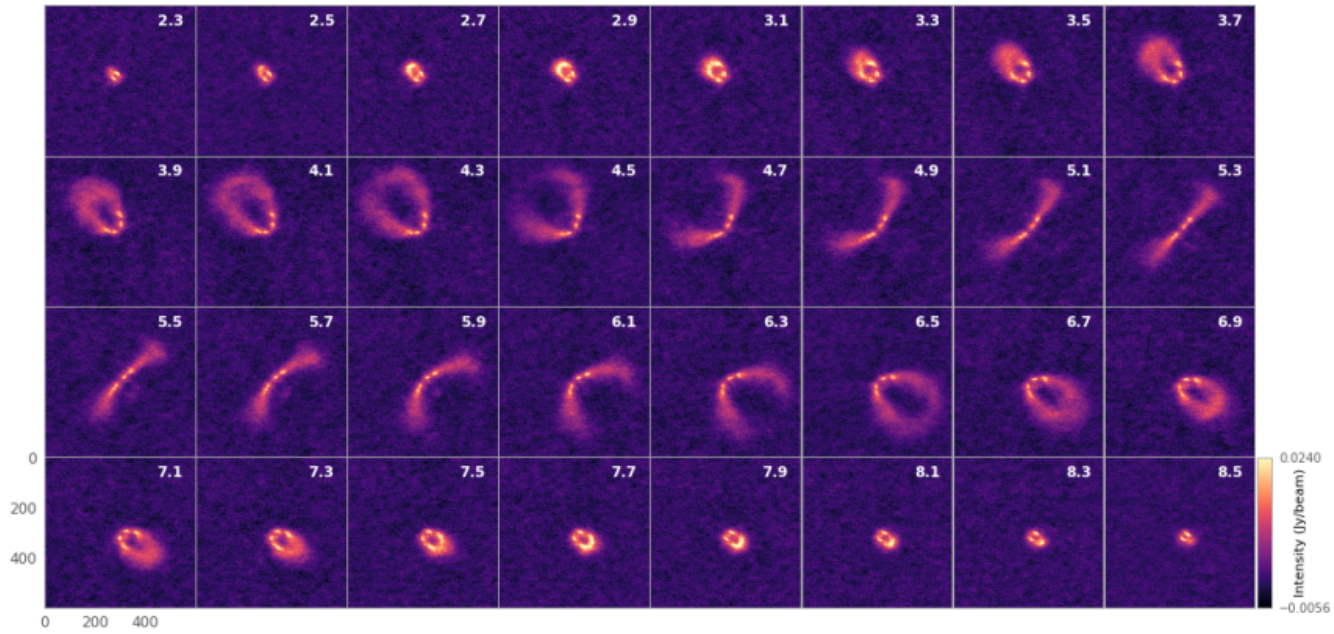

Figure 2.5: The figure shows the Channel map for the HCN line for band 6 (J=3-2) and includes a color bar of the intensity flux. For this figure, the minimum and maximum intensity values are -5.6 and 24.0 mJk/beam respectively.

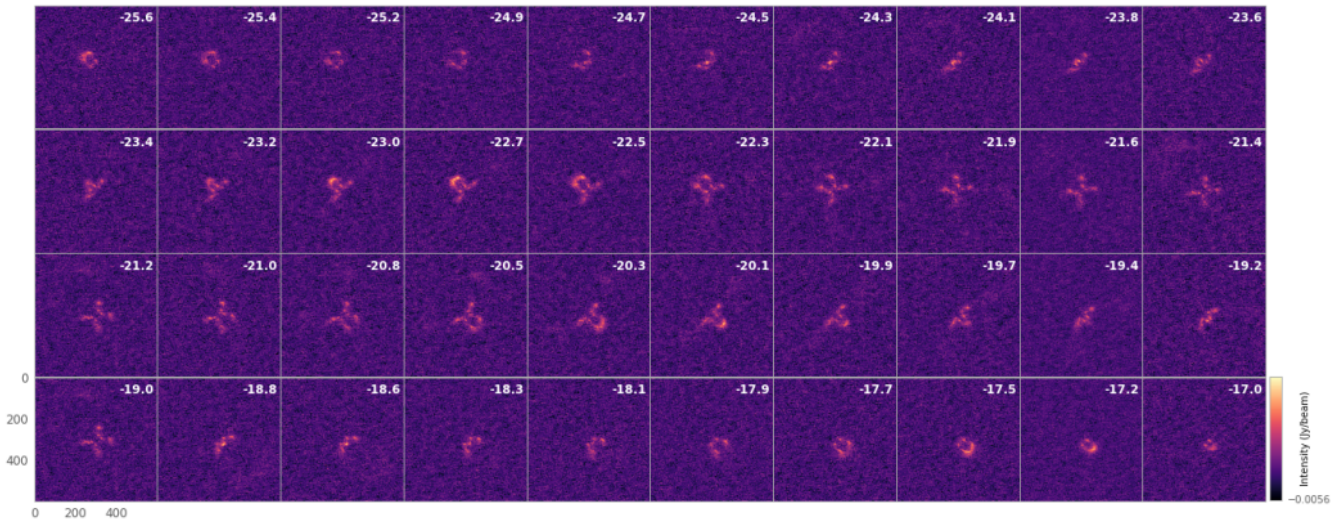

Figure 2.6: The figure shows the Channel map for the C_2H line for band 6 ($J = 3 - 2$) and includes a color bar of the intensity flux. For this figure, the minimum and maximum intensity values are -6.0 and 20.0 $mJk/beam$ respectively.

In the next section, the methodology used for the parameterization of the models in the structure of the molecular gas seen in the protoplanetary disk HD 163296 will be discussed, in addition to the method for calculating the radiative transfer of HCN and C_2H in the disk. For modeling, the cleaned data provided in this section will be used. If you need to know more about how these interferometric data are obtained and their theory, review the appendix A.

Chapter 3

Methodology

In this chapter, the details about the methodology used to model the emission of the molecules HCN and C_2H in the protoplanetary disk HD 163296 will be described. This research aims to analyze the vertical and radial distribution of these molecules. To achieve this, we will seek to parameterize the abundance of HCN and C_2H concerning molecular hydrogen H_2 through synthetic models, calculating the radiative transfer of the emission and then comparing it with the observations made by MAPS.

3.1 Deprojected Radial Profiles

To analyze the structure of the disk HD 1263296, one of the most important tools that can be used is radial profiles. Radial profiles provide detailed information about the distribution of material, such as dust and gas, within the disk. This is crucial for understanding the overall structure of the disk and how it evolves.

Radial profiles can reveal distinctive features such as rings, gaps, and other substructures (Diep et al. (2019)). These features may indicate ongoing physical processes, such as planet formation, interactions with companion stars, or effects of disk winds. Radial profiles can show evidence of planet formation, where forming planets may create gaps or rings in the disk as they accumulate material (Rab et al. (2020)). Understanding these profiles helps to identify potential sites of planetary formation and to better understand how planets form and evolve in these environments.

When analyzing radial profiles from different spectral lines, information about the physical conditions (temperature, density) and chemical conditions (chemical composition) of the disk at different radii can be obtained. Moreover, comparing observational radial profiles with theoretical models helps to validate and refine models of protoplanetary disks and theories of planet formation.

The **GoFish**[1] (Teague (2019)) package in Python is a specialized tool for analyzing observations of protoplanetary disks, particularly those obtained with interferometers like ALMA (Atacama Large Millimeter/submillimeter Array). GoFish is designed to extract radial or azimuthal intensity profiles from high-resolution images of protoplanetary disks.

Here is an overview of how GoFish works and what you can do with it:

- Load Data: GoFish can read interferometry data, like those produced by ALMA. These data are usually in FITS format and contain information about the intensity of radiation at different wavelengths coming from the protoplanetary disk. The code uses GoFish's imagecube to load observational data from the protoplanetary disk HD 163296. Different datasets are loaded from FITS files located at a specified path.

- Definition of Disk Geometry: It is necessary to define the disk's geometry, including its inclination, angular position, and distance. This is crucial as GoFish calculates the radial and azimuthal profiles based on this geometry. Using GoFish's $radial\_profile$ method, the code calculates the radial profiles for each dataset. Here, disk parameters such as inclination (inc), angular position (PA), star mass ($mstar$), and distance ($dist$) are specified. These profiles represent how the integrated intensity (in $Jy/beam\ km/s$) varies as a function of the disk's radius.

- Extraction of Intensity Profiles: With the geometry defined, GoFish extracts the radial or azimuthal intensity profiles from the disk. This means measuring how the intensity of the radiation changes with the distance from the center of the disk or along a particular angle. Matplotlib is used to create a graph that displays the radial profiles. Different colors and labels are used to differentiate between observations and various models.

- Analysis and Visualization: The extracted profiles can be analyzed to study different features of the disk, such as the presence of gaps, rings, or spiral structures.

The radial profiles extracted for the protoplanetary disk HD 163296 for the molecules HCN and C_2H can be visualized in Figure 3.1. The parameters used were $inc = 46.7$, $PA = 133.3$, $mstar = 2.0$ (solar masses), and $dist = 101.0$ (parsecs).

[1] https://github.com/richteague/gofish

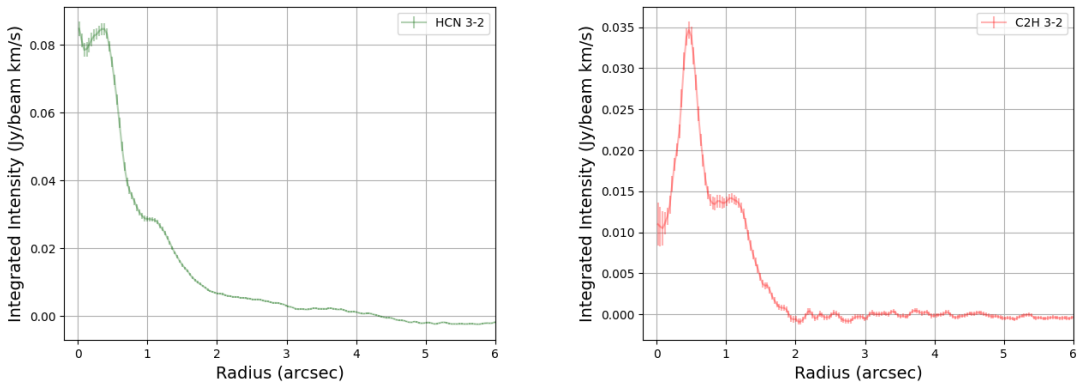

Figure 3.1: The figure shows the radial profiles of the disk HD 163296. The figure on the left displays the relationship between the integrated intensity as a function of the radius for the molecule HCN in the 3-2 transition. On the right, the relationship between the integrated intensity as a function of the radius for the molecule C_2H in the 3-2 transition is shown. Both molecules exhibit a particular structure of bright rings.

GoFish generates the error bar using the statistical uncertainty of the measurements at each point of the radial profile. The $radial\_profile$ function of GoFish not only calculates the average intensity in concentric rings around the center of the disk, but it can also calculate the standard deviation of the intensity within each ring.

The intensity is measured in a series of pixels that form a ring around the center of the disk. The average value of the intensity is calculated for all the pixels within that ring. The standard deviation of the intensities is calculated to estimate the dispersion of the values around the mean. The standard deviation can be interpreted as the uncertainty of the intensity measurement in that specific ring, which is what dy represents. The standard deviation (dy) is used to draw the error bars on the graph of the radial profile, representing the uncertainty associated with each data point.

3.2 Abundance retrieval

Several modeling approaches have been developed to interpret interferometric molecular lines and continuous disk observations (Dutrey et al. (2014)). The power law is a widely used mathematical tool in astrophysics and other disciplines to model a variety of natural phenomena, including the physical structure of protoplanetary disks. This law describes the functional relationship between two variables. In our particular case, we aim to model the molecular abundance of HCN and C_2H as a power law in the following way:

$$X = X_1(\frac{r}{R_0})^{\alpha} \tag{3.1}$$

where X_1 is the abundance relative to total hydrogen at a radius of 100 au (R_0), r is the distance from the star in au, and α is a power-law index. Additionally, we assume that HCN and C_2H are present with a constant abundance in a layer with boundaries toward the mid-plane and toward the surface of the disk, these two vertical limits, Z/R low and Z/R upper. Finally, we included an outer cutoff radius R_{out}. This parametrization is a common approach when modeling molecular abundances in disks (e.g., Guzmán et al. (2017), Qi et al. (2008) and Qi et al. (2013)).

3.2.1 Parametric model

In this research, we aim to parameterize the overall structure of the disk and its substructures. We define the general structure of the disk by parameterizing the relative abundance of HCN and C_2H with respect to H_2 as a power law. As seen earlier, the radial profiles provide us with important information on how the structure of HCN and C_2H would be distributed.

In a simplified scenario, we might assume a direct proportional relationship between abundance and integrated intensity, in order to compare the radial profiles of the observations with the profile of relative abundance. However, it's important to note that this is a simplification and that in reality, the relationship might be more complex.

To model the distribution of relative abundance in the protoplanetary disk HD 163296, we have used an approach that combines a power law with superpositions of Gaussian functions. The power law describes the decreasing trend of abundance with distance from the central star, and the Gaussian functions represent bright rings indicating localized concentrations of material.

Power law for the general structure of the disk:

- The power law states that the relative abundance X varies with the radius r from the central star according to the equation $X = X_1(r/R_0)^{\alpha}$, where X_1 is the relative abundance at a reference radius R_0, and α is the power law index that describes how the abundance changes with the radius.
- In our example model, shown in Figure 3.2 below, the value of X_1 is set at 1x10^{-11}, the reference radius R_0 is 100 au, and the power index α is -0.2. This implies that the relative abundance decreases with the distance from the star, like radial profile, behavior similar to those shown in the radial profiles of HCN and C_2H.

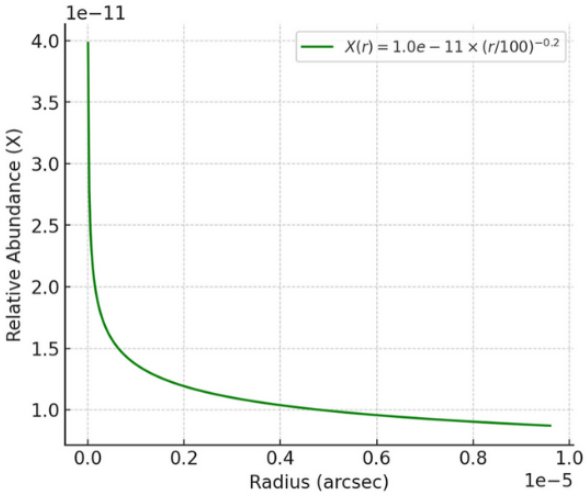

Figure 3.2: The figure shows a parameterized model of relative abundance as a power law.

Bright Rings Parameterized by Gaussian Functions:

- Bright rings are modeled by superimposing Gaussian functions on the power law distribution of abundance. Each Gaussian is characterized by three parameters: the amplitude Amp_n, the width σ_n, and the central position R_n.

- The amplitude of the Gaussian Amp_n is calculated as a percentage A_n of the abundance X at a specific radius, determined by the power law. The amplitude of the Gaussian is:

$$Amp_n = A_n(X_1(r/R_0)^{\alpha}) \tag{3.2}$$

- The shape of the Gaussian is described by

$$G_n = Amp_n \; exp\left(-\frac{(r-R_n)^2}{2\sigma_n^2}\right) \tag{3.3}$$

  where r is the radial distance from the central star.

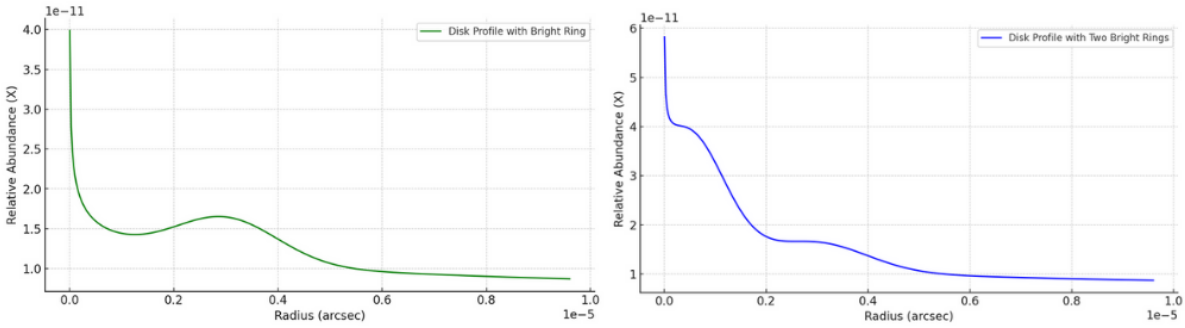

Figure 3.3: The figure on the left shows the model superimposing the power law and a Gaussian function as a ring (G_1). The parameters used were: A_1=0.5, scaling the abundance to 50% of X_1 at the peak of the ring, R_1=0.3×10^{-5} arcseconds, and σ_1=0.1×10^{-5} arcseconds, defining the width of the ring. The figure on the right shows the model superimposing the power law and two Gaussian functions as rings (G_1 and G_2). The parameters used were: A_2=1.5, scaling the abundance to 150% of X_1 at the peak of the ring, R_2=0.05×10^{-5} arcseconds, and σ_2=0.07×10^{-5} arcseconds, defining the width of the ring.

The result shown in Figures 3.2 and 3.3 is an abundance profile that displays the general decreasing structure of the disk with peaks where the bright rings are located, reflecting a higher concentration of material at those specific radii. This model can be adjusted and may be a good approximation for comparing real observations and synthetic models. In the next section, the method for calculating radiative transfer using this structure to model the HD 163296 disk more accurately will be shown, in order to better understand the distribution of material around protoplanetary disks.

3.3 Radiative transfer: RADMC-3D

Radiative transfer refers to the process by which electromagnetic radiation moves through space and interacts with matter along our line of sight. Radiative transfer is fundamental to understanding how light propagates through different media and how it affects the objects we observe, such as stars, protoplanetary disks, nebulae, and galaxies. The theory of radiative transfer is detailed in the appendix C.

RADMC-3D[2] is an astrophysical simulation code used to model radiation and particle transport in dense and dusty environments in stellar and planetary settings. Primarily, it allows for comparing parameterized models with observational data. The applications of RADMC3D are extensive and enable its use in different types of objects such as protoplanetary disks (Calahan et al. (2022), Liu et al. (2018)), molecular clouds, dust around

[2] https://www.ita.uni-heidelberg.de/~dullemond/software/radmc-3d/

active galactic nuclei, circumstellar environments, and other scenarios (Dullemond et al. (2020)). Additionally, the code has the capability to perform simulations in three spatial dimensions.

RADMC-3D uses the Monte Carlo method to simulate the transport of radiation and particles through the dusty medium. This method involves tracing a large number of fictitious photons or particles through space and tracking their interactions with the dust. This simulation allows for modeling complex astrophysical structures in three dimensions, which is essential for studying realistic stellar and planetary environments.

The Monte Carlo method is based on random sampling. Instead of solving a radiative transfer equation analytically or using a regular grid, the Monte Carlo method simulates the behavior of individual photons or particles as they interact with the medium. Fictitious photons or particles are generated to represent the radiation or particles under study. These fictitious photons propagate through the dusty medium in successive steps and experience interactions with the dust along their path. At each step, a random decision is made about what happens to the fictitious photon or particle. This can include scattering, absorption, emission, or any other interaction relevant to the problem at hand. The probabilities of these interactions are determined from the properties of the medium and dust particles.

As a large number of fictitious photons are simulated and their interactions along their trajectories are recorded, these statistics accumulate significantly. This allows for the calculation of macroscopic properties such as the radiation flux density at a given point, the observed spectrum, temperatures, or parameters related to the structures of stellar objects.

The accuracy of Monte Carlo results depends on the number of simulated fictitious photons. The larger the number of simulated photons, the more accurate the solution will be. This is because the Monte Carlo method is stochastic and relies on statistics.

Below is a brief description of the inputs and functioning of RADMC-3D that has been used for the calculation of radiative transfer:

- With RADMC-3D we can define the structure of the spatial grid where the calculations will be carried out, establishing the basis of the geometry on which all physical properties are mapped. The resolution and spatial extent are defined, affecting the assignment of physical properties such as density and temperature.
- Density and temperature profiles describe how the temperature and velocity of the gas vary throughout the disk, affecting how the gas dynamics are modeled. They are fundamental for calculating radiative transfer and for predicting the spectral lines and the synthetic image of the disk.

- Define the number density (Molecular hydrogen H_2). These values directly affect the emission and absorption of radiation and are key to simulating spectral lines. Using the number density information, the program performs radiative transfer calculations to simulate how light interacts with the disk.

- Microturbulence defines a microturbulence velocity throughout the disk, which is important for the broadening of spectral lines and for radiative transfer calculations.
- Spectral lines, specify the spectral lines to be simulated. The frequencies used for these lines are critical, as they must match the energy transitions of the molecules.
- Define the molecular properties, this contains data about the molecule, HCN or C_2H, that RADMC-3D uses to simulate how this molecule emits and absorbs radiation and its collision rates. These values are directly extracted from catalogs (**LAMDA**[3]).
- Define the structure of the synthetic models to be modeled.

Models of the gas structure. In this case, it is defined that the abundance model, for the species HCN and C_2H, is parameterized using a combination of power laws to simulate the general structure of the disk, and Gaussian functions to simulate bright rings. In the context of RADMC-3D for modeling protoplanetary disk HD 163296, the mentioned parameters are described as follows:

- Z/R *low* and Z/R *uppper*: Set the vertical limits in the disk model, defining the height or thickness of the disk region that is being simulated.
- α: It is the index that describes how certain properties, such as dust density or temperature, change with the distance from the central star, directly affecting the structure and appearance of the disk.
- X_1: Represents the initial concentration or relative abundance of a particular species at a reference point in the disk, crucial for simulating molecular emission and absorption.
- R_n: These are specific radial positions that identify features such as rings or gaps in the disk, allowing for detailed modeling of its structure.
- σ_n: Determines the width of the Gaussian functions that model the bright rings, influencing how these features are distributed along the disk.
- A_n: Modify the intensity of the bright rings in the model, affecting the visibility and prominence of these structures in the simulated images and spectra.

[3] https://home.strw.leidenuniv.nl/~moldata/

We run each model and evaluate the fit by comparing it with observational data. Finally, in this astrophysical context and specifically in simulations like RADMC-3D, emcee will be used, which is a Python library for performing Markov Chain Monte Carlo (MCMC) sampling, commonly used for fitting synthetic models and for parameter optimization based on observations.

3.4 Model fitting with emcee

The **emcee**[4] (Foreman-Mackey et al. (2013)) is a Python library used for Markov Chain Monte Carlo (MCMC) sampling. MCMC is a statistical technique employed to estimate posterior probability distributions in Bayesian inference problems. Emcee is a popular tool for conducting this type of analysis in Python.

The term "emcee" is an abbreviation for "Ensemble MCMC," indicating that it uses an ensemble sampling approach to efficiently explore the parameter space. Unlike some other MCMC methods that follow a more traditional approach in parameter space exploration, Emcee employs multiple simultaneous Markov chains to do so. This strategy can expedite convergence and provide a more accurate estimation of the posterior distribution.

Emcee allows for efficient fitting of the parameters of the protoplanetary disk model (in this case, the molecule's abundance, the parameters of the general structure, and the parameters of the bright rings) so that the simulations align as closely as possible with the actual observations.

Functionality of emcee:

- Firstly, you need to define the statistical model you are trying to fit to your data. This involves specifying the prior probabilities and the likelihood function that describes the probability of observing your data given the conditions of the model.
- You have to set up the Markov chains that the emcee will use to explore the parameter space. This involves defining the number of chains, the length of each chain, and possibly other tuning parameters.
- Initial values are needed for each Markov chain. These initial values are typically either generated randomly or can be set manually.
- Emcee will sample the Markov chains to explore the parameter space. It employs the Metropolis-Hastings algorithm to propose new points in the parameter space and decides whether to accept or reject them based on posterior probabilities.

[4] https://emcee.readthedocs.io/en/stable/

- Once the Markov chains have converged, you can examine the samples to obtain estimates of the parameters of interest and their uncertainties.

These are some important terms and concepts associated with using the emcee library in Python:

- Walkers: The "Walkers" are the Markov chains that Emcee uses to explore the parameter space. In emcee, you can define the number of walkers that will be used for sampling. The number of walkers is usually greater than the number of dimensions in your parameter space, which helps explore the space more effectively. A higher number of walkers can improve convergence and provide a more accurate estimation of the posterior distribution.

- nchunks: "nchunks" refers to the number of chunks or blocks into which the total set of MCMC iterations is divided. This feature is used to parallelize the sampling process, which can significantly speed up the runtime, especially on systems with multiple CPU cores.

- niter: "niter" refers to the number of iterations that will be run for each walker in the MCMC process. A larger number of iterations generally allows for better exploration of the parameter space but can also increase runtime. It's important to balance the number of iterations with computational efficiency and algorithm convergence.

- Threads: The "Threads" refer to the execution threads in a parallel program. The emcee offers the option to run MCMC in parallel using threads instead of independent processes. This can be beneficial on systems with multiple CPU cores and may enhance the efficiency of the sampling process.

- Corner Plots: "Corner plots" are graphs that display marginal distributions and pairwise relationships between estimated parameters from MCMC samples. These plots are useful for visualizing uncertainty in parameters and identifying correlations among them. In emcee, you can use libraries like "corner.py" to easily generate these plots.

- Plot of iterations with results: This type of plot shows how the parameter values evolve over the iterations of MCMC. This visualization can be used to assess the convergence of the algorithm and observe how parameter values stabilize as the sampling process progresses. You can generate these plots using the parameter samples generated by emcee and visualization libraries like Matplotlib.

In addition to finding the best parameters, the emcee helps to estimate the uncertainty in these parameters, providing a more complete understanding of the model's accuracy.

3.4.1 Uncertainties

To obtain uncertainties from a corner plot generated by emcee (or other Monte Carlo sampling libraries), we can use the quantiles shown in the corner plot. The quantiles will provide you with estimates of the uncertainty intervals for your parameters (Foreman-Mackey et al. (2013)).

A common approach is to use the 16th, 50th, and 84th percentiles, where the 50th percentile represents the median of the parameter, and the difference between the 84th and 50th percentiles, and between the 50th and 16th percentiles, provides the upper (δ_u) and lower (δ_l) uncertainties, respectively. This results in a 68% credibility interval (equivalent to one standard deviation if the distribution is Gaussian) that reflects the asymmetric uncertainty around the median value.

For example, if in the corner plot, for a parameter X, the quantile values are $X_{0.16}$ for the 16th percentile (0.16), $X_{0.5}$ for the median (Percentile 50 or 0.50), and $X_{0.84}$ for the 84th percentile (0.84). Then, the uncertainty for the parameter X would be:

$$\begin{aligned} \delta_u &= X_{0.84} - X_{0.5} \\ \delta_l &= X_{0.5} - X_{0.16} \end{aligned} \tag{3.4}$$

This means that the most probable value for the parameter X is $X_{0.5}$, with an uncertainty of $+\delta_u$ and -δ_l around that value or $X^{+\delta_u}_{-\delta_l}$. This calculation can be applied to each of the parameters in the analysis to obtain their corresponding uncertainty intervals. It should be noted that this is an estimate of uncertainty based on the distribution of your sampling data and the assumption that they follow a Gaussian distribution. If the distributions are highly asymmetric or non-Gaussian, more advanced methods for obtaining uncertainties, such as error propagation techniques, may need to be considered (Hogg et al. (2010)).

The quantiles argument in the corner plot refers to the quantiles that will be shown on the corner plot. Quantiles are values that divide a distribution of data into equal portions. In this case, three quantiles are being specified: 0.16, 0.50, and 0.84.

- 0.16 corresponds to the 16th percentile, meaning it represents the value where 16% of the data fall below and 84% are above. This quantile is commonly used to calculate lower bounds of confidence intervals
- 0.50 corresponds to the 50th percentile, which is the median of the data and separates the distribution into two equal parts. It is the value where 50% of the data falls below

and 50% is above.

- 0.84 corresponds to the 84th percentile, meaning it represents the value where 84% of the data fall below and 16% are above. This quantile is commonly used to calculate the upper bounds of confidence intervals.

In the context of the corner plot, these quantiles are used to display typical or median values of the parameters in the data analysis, along with uncertainty intervals. The quantiles can be customized according to needs or preferences.

In a corner plot (also known as a corner plot or joint distribution plot), the histograms on the main diagonal represent the marginal distributions of each parameter in your analysis. Each histogram shows how the values of a specific parameter are distributed when the other parameters are held constant.

For example, if you have a corner plot with 4 parameters (A, B, C, D), the main diagonal would contain 4 histograms. The upper-left histogram would show the distribution of values for A, keeping the values of B, C, and D fixed. The upper-right histogram would show the distribution of values for B, keeping the values of A, C, and D fixed. The other two histograms on the main diagonal would operate similarly for parameters C and D.

The plots off the main diagonal (scatter plots in the upper triangle and density plots in the lower triangle) represent the joint relationships between pairs of parameters. These plots show you how the parameters are correlated and how they change together based on the sampling data.

In summary, the histograms on the main diagonal of the corner plot are useful for visualizing the marginal distributions of each parameter, while the plots off the main diagonal show the joint relationships between parameters. This is especially helpful for understanding covariation and correlations between parameters in a data analysis.

Chapter 4

Results

In this section, the main results of this research are summarized. As we saw in the previous section 3.1, we can model the observed structure by parameterizing the relative abundance of HCN and C_2H. In our case, we used toy models to manually estimate the input parameters of the model. Then, using RADMC-3D to calculate the radiative transfer of the structure and using the tclean task to clean the generated models and create .fits files similar to those of the observations. Finally, GoFish calculates the deprojected profiles of the synthetic model and compares them to those of the observations.

Due to the number of parameters in the model (three for the general structure and nine for the bright rings of the disk's substructure), the process was divided into two parts:

- First, through toy models, we estimate the input parameters for the general structure parametrization of HD 163296 using the power-law approach. Then, using these parameters ($Z/R\ low$, X_1, and α), we use the **emcee** Python package to determine the best-fit parameters for the synthetic model that best matches with the observations for the molecules HCN and C_2H. For HCN, three different tests were conducted, using $Z/R\ low$ as a fixed parameter and X_1 and α as free-fit parameters. For C_2H, a single test was performed, with all three parameters set as free parameters.

- Second, once the parameters for the general disk structure were obtained from the previous step, input parameters for the bright rings of the disk's substructures were estimated using toy models with Gaussian functions. Subsequently, using these parameters, emcee was used to determine the best synthetic model that best fits the observation data. For both molecules, HCN and C_2H, a single test was performed, leaving the molecule's abundance (X_1), ring positions (R_n), ring widths (σ_n), and scale factor of ring amplitudes (A_n) as free-fit parameters.

When estimating the emission height $Z/R\ low$ for HCN and C_2H using ALMA data in bands 6 and 3, we take advantage of the difference in both upper-level energies and

in angular resolution between these bands. Band 6, with a higher frequency, can provide finer resolution, while band 3 can penetrate deeper into the disk because lines have lower upper energies and therefore trace colder gas. With observations at only two frequencies, it is assumed that the distribution of the molecules' emission follows a trend that can be extrapolated to other frequencies. This is why, to achieve greater precision in calculating the height of the disk, we use both sets of data, bands 3 and 6. However, for modeling the substructures, we only use the higher resolution data (band 6), where the substructures are much more noticeable than in band 3.

4.1 General gas structure

Below are the results obtained from the synthetic models of the general structure of the disk using the power law, to determine the input parameters, X_1, α, and $Z/R\ low$, and finally generate the synthetic models of the general structure and the substructures of bright rings observed in HD 163296.

Using the Python package emcee, the goal is to find the best parameters for the synthetic model to fit the observational data. Specifically for the molecule HCN, the parameter Z/R low was kept fixed, and the free parameters explored were the molecule's relative abundance (X_1) and the power-law parameter α. Three tests were conducted using different values of $Z/R\ low$ (0.07, 0.09, and 0.11). Initial values obtained from the toy models were used to explore the parameter space of X_1 and α with the emcee. For C_2H, a single test was performed, with all three parameters, $Z/R\ low$, X_1, and α, set as free-fit parameters.

After the model is fitted using MCMC, different figures emerge for the analysis of the results as you can see in the figures 4.2, 4.1, 4.3. The **walker** graphs show different MCMC chains exploring the parameter space. The initial values of the parameters were determined from the toy models. Each walker takes steps through the parameter space, selecting new points based on the posterior probability function. The **corner** plots are multi-dimensional graphs that show the distributions of all pairs of parameters. They help to visualize the correlations between parameters and the shape of the complete posterior distribution. The contours in the corner plot represent regions of increasing probability. The innermost contours enclose regions of higher probability density, indicating that the parameter values within those contours are more consistent with the data, given the model assumptions. Finally, the **histograms** show the distribution of sampled values for each parameter, we use them to understand the posterior distribution of the parameters. The obtained values and their uncertainties are shown in the following table 4.2.

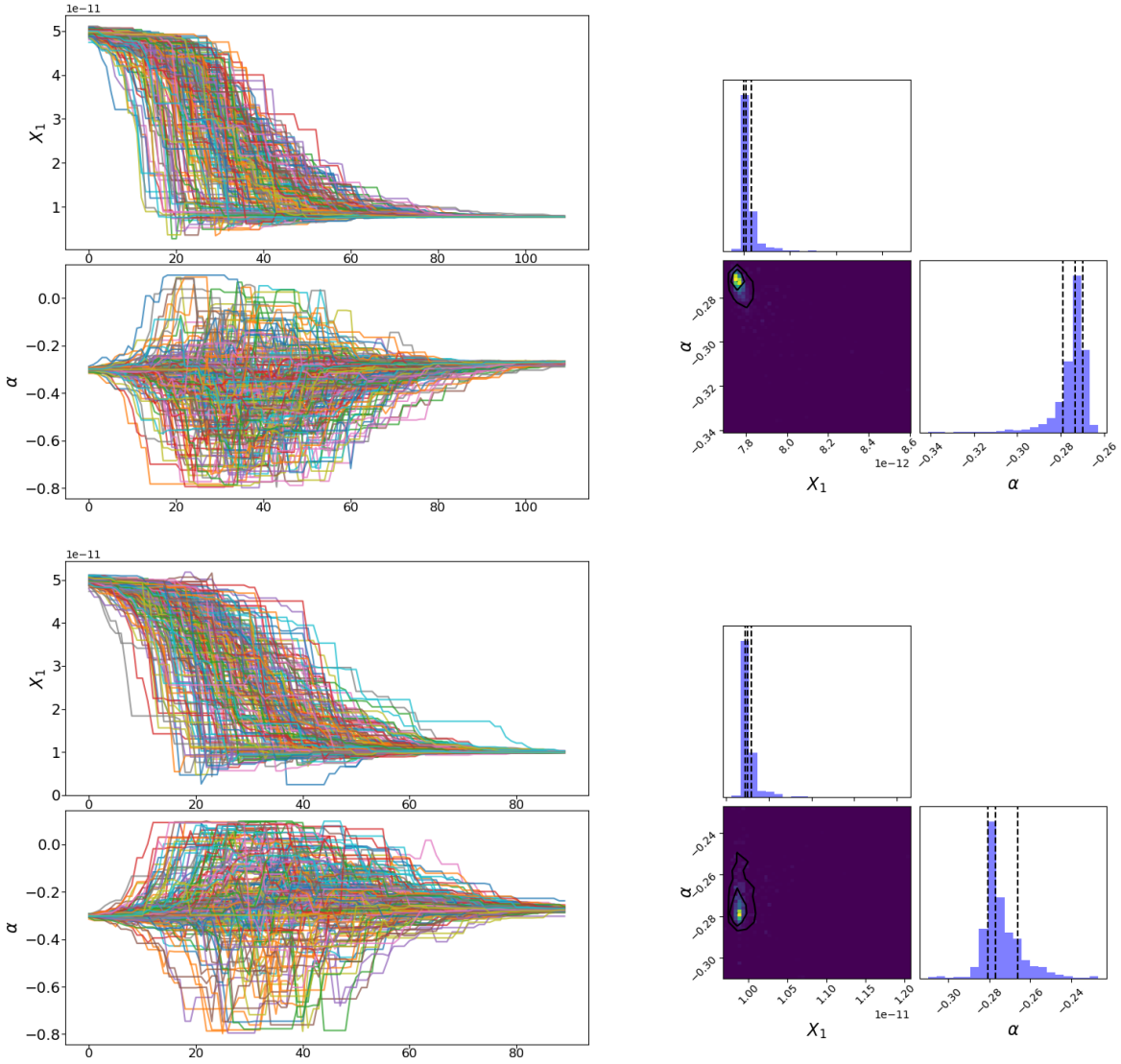

Figure 4.1: The figure shows the fit results obtained using $Z/R\ low = 0.07$ (top figures), and $Z/Rlow = 0.09$ (lower figures) as a fixed parameter for the HCN molecule. Left: The figures show how the walkers evolve over the iterations that the emcee uses to explore the parameter space, X_1, and α parameters. The number of walkers used was 100 for both cases in 110 and 90 iterations, respectively. Right: The figures show the "corner plots" that show the marginal distributions and the correlation between the pair of parameters estimated from the emcee samples. The dashed vertical lines correspond to the 16th, 50th, and 86th percentiles respectively.

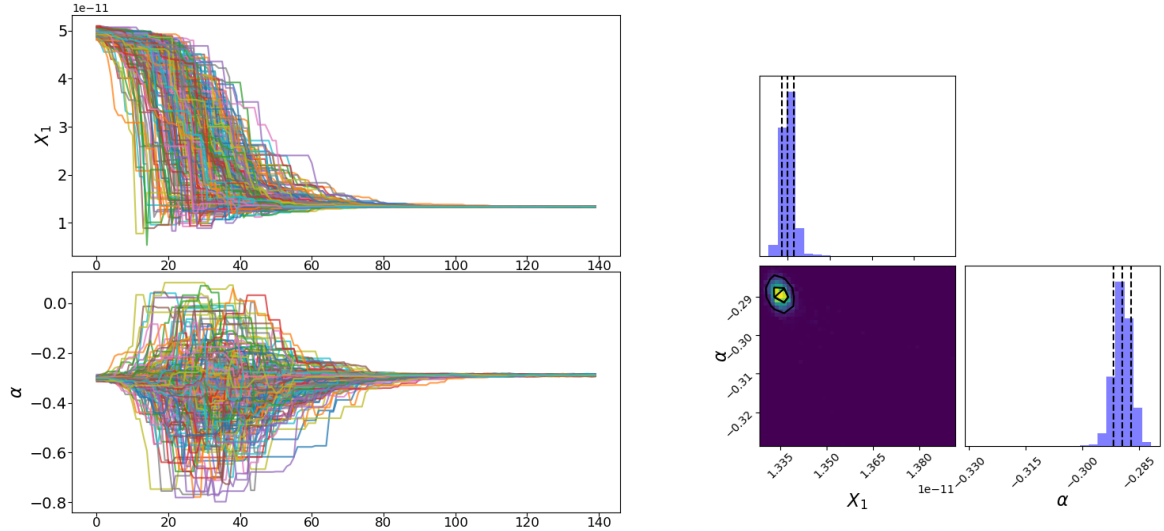

Figure 4.2: The figure shows the fit results obtained using $Z/R\ low = 0.11$ as a fixed parameter for HCN molecule. Left: The figure shows how the walkers evolve over the iterations that the emcee uses to explore the parameter space, in this case, X_1 and α. The number of walkers used was 100 in 140 iterations. Right: The figure shows the corner plots that show the marginal distributions and the correlation between the pair of parameters estimated from the emcee samples. The dashed vertical lines correspond to the 16th, 50th, and 86th percentiles respectively.

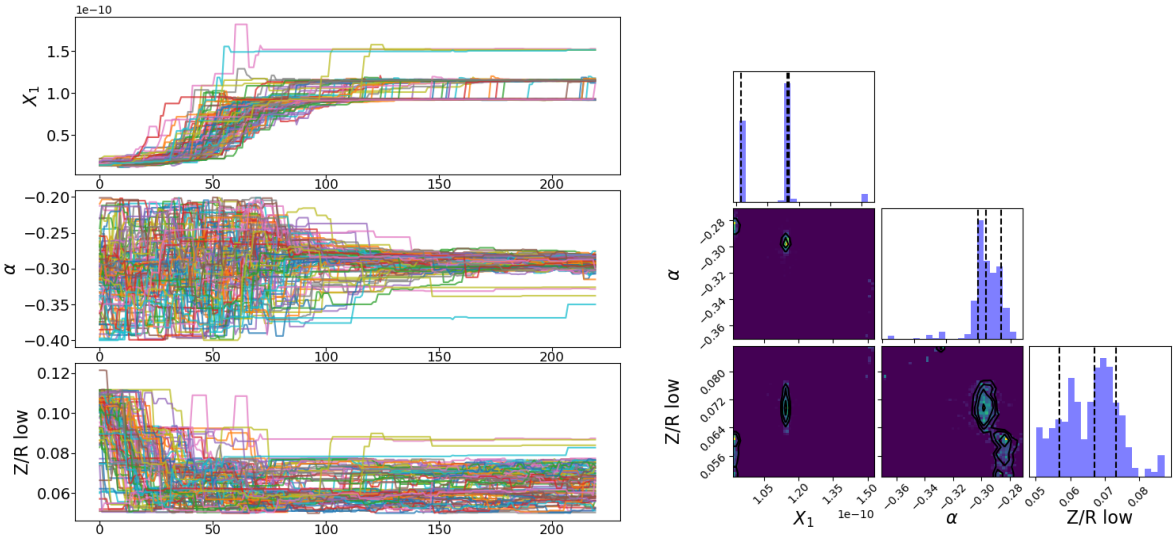

Figure 4.3: The figure shows the fit results obtained for C_2H molecule. Left: The figure shows how the walkers evolve over the iterations that the Emcee uses to explore the parameter space, $Z/R\ low$, X_1, and α. The number of walkers used was 100 in 220 iterations.

Species	$Z/R\ low^{+\delta Z/Ru}_{-\delta Z/Rl}$	$\alpha^{+\delta\alpha u}_{-\delta\alpha l}$	$X_1{}^{+\delta Xu}_{-\delta Xl}$
HCN	0.07	$-0.273^{+0.003}_{-0.006}$	$7.77\text{e-}12^{+0.03}_{-0.01}$
	0.09	$-0.277^{+0.01}_{-0.003}$	$9.89\text{e-}12^{+0.05}_{-0.03}$
	0.11	$-0.289^{+0.002}_{-0.002}$	$1.34\text{e-}11^{+0.02}_{-0.02}$
C_2H	$0.067^{+0.006}_{-0.01}$	$-0.294^{+0.01}_{-0.006}$	$1.1\text{e-}10^{+0.7}_{-0.2}$

Tabla 4.1: The table shows the values and uncertainties of the parameters $Z/R\ low$, X_1 and α obtained after fit using the emcee method. For HCN three tests use $Z/Rlow$ as fixed parameters. Furthermore, for the C_2H molecule, the three parameters were used as free parameters in the fit. These are the parameters used to determine the complete structure of the HD 163296 disk for both molecules.

Species	$Z/R\ low^{+\delta Z/Ru}_{-\delta Z/Rl}$	$\alpha^{+\delta\alpha u}_{-\delta\alpha l}$	$X_1{}^{+\delta Xu}_{-\delta Xl}$
HCN	0.11	$-0.289^{+0.002}_{-0.002}$	$1.34\text{e-}11^{+0.02}_{-0.02}$
C_2H	$0.067^{+0.006}_{-0.01}$	$-0.294^{+0.01}_{-0.006}$	$1.1\text{e-}10^{+0.7}_{-0.2}$

Tabla 4.2

For HCN, the criterion used to choose the optimal value of the $Z/R\ low$ parameter for use in the complete disk structure was:

- Through the residual values compared between the original observation images and the synthetic models generated. As shown in Figure 4.4, the model with the best residual value is shown by $Z/R\ low = 0.11$ with an SNR of 4.1, or 4.1σ, while the other models have residual of 4.5 and 4.6σ, for $Z/R\ low = 0.09$ and $Z/R\ low = 0.07$ respectively.
- On the other hand, the radial profiles show that the integrated intensity curve that could best represent the intensity emission of the observation is also the model with the value of 0.11, as seen in Figure 4.5, although the difference is not too large in this graph.

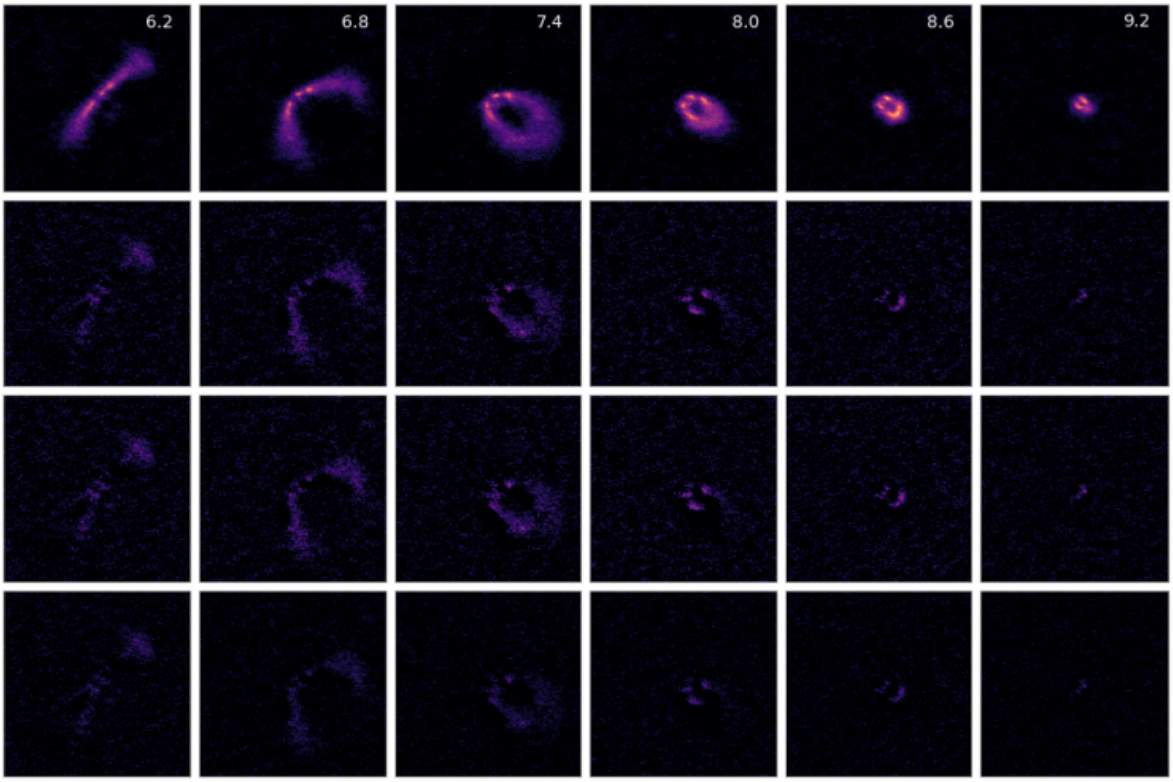

Figure 4.4: The figure shows the channel map for the HCN line. In the top row, the observation channels for Band 6 ($J = 3-2$) are displayed. In the second, third, and fourth rows, the channel map resulting from the residuals between the synthetic models and the observation for each value of Z/R *low* used, 0.07, 0.09, and 0.11, respectively, are shown. The range of the residual values for Z/R *low*=0.07 is 9.9σ to 4.6σ. The range for Z/R *low*=0.09 is 9.9σ to 4.5σ. Finally, for Z/R *low*=0.11 is 8.7σ to 4.1σ.

For C_2H, the criterion used to choose the optimal values of the Z/R *low* and α parameters was from the best model after fitting with MCMC shown in the figure 4.3. The radial profile using the parameters of the best model is shown in Figure 4.5 on the right. The integrated intensity curve representing the emission intensity of the observation is expected to improve from the modeling with the substructures, as these contain most of the emission in the disk for C_2H.

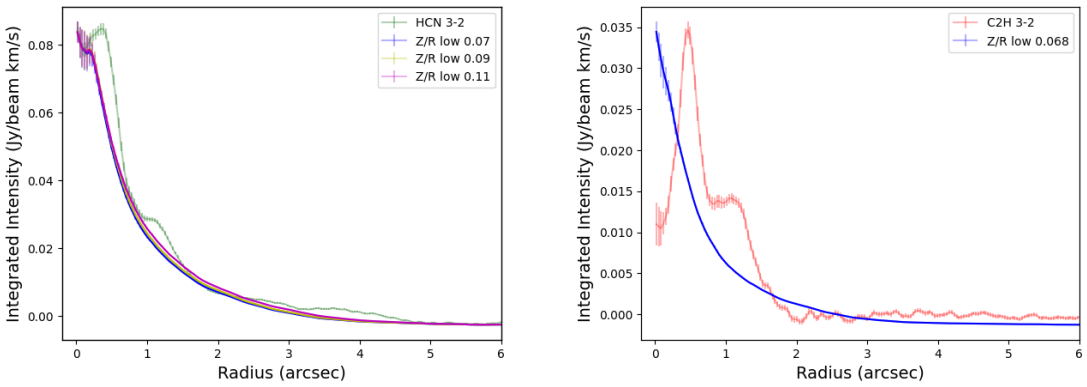

Figure 4.5: The figure shows the radial profiles of the moment-zero of the observation data in Band 6 for the HCN molecule and the synthetic models (Left) and C_2H (Right). The horizontal axis represents the distance from the center of the HD 163296 disk, and the vertical axis shows the integrated intensity. The synthetic models were generated using the values from Table 4.2, employing a power-law as the general disk structure parametrization.

4.2 Bright rings as substructures in molecular gas.

In this subsection, the results generated by the synthetic models for the substructures of the HD 163296 disk are presented. The bright rings were modeled using Gaussian functions as a parameterization and added to the general disk structure shown earlier. The synthetic models kept the parameters Z/R *low* and α fixed, using values obtained previously with the fit on general structure (Table 4.2). On the other hand, the abundance X_1 and the parameters of the respective Gaussian function for each bright ring as free parameters.

For both the HCN and C_2H molecules, the synthetic models of the entire disk structure were based only on the observations in Band 6. This is because this is where the substructures in HD 163296 are best seen and the images have the highest resolution. From this point onward, the modeling for both molecules is the same, seeking to generate the best set of parameters that can represent the observations in the disk. 3 bright rings were modeled using Gaussian functions, which represent the position of the ring (R_n), the width of the ring (σ_n), and how its relative abundance increases concerning the power law through a scaling factor (A_n). Figures 4.6, 4.8 and 4.7, 4.9 show the results of the evolution of the walkers exploring the parameter space and the corner plots. Figures 4.10 show histograms representing the statistical weights of each parameter and their correlation with the other fitted free parameters for HCN and C_2H molecules respectively.

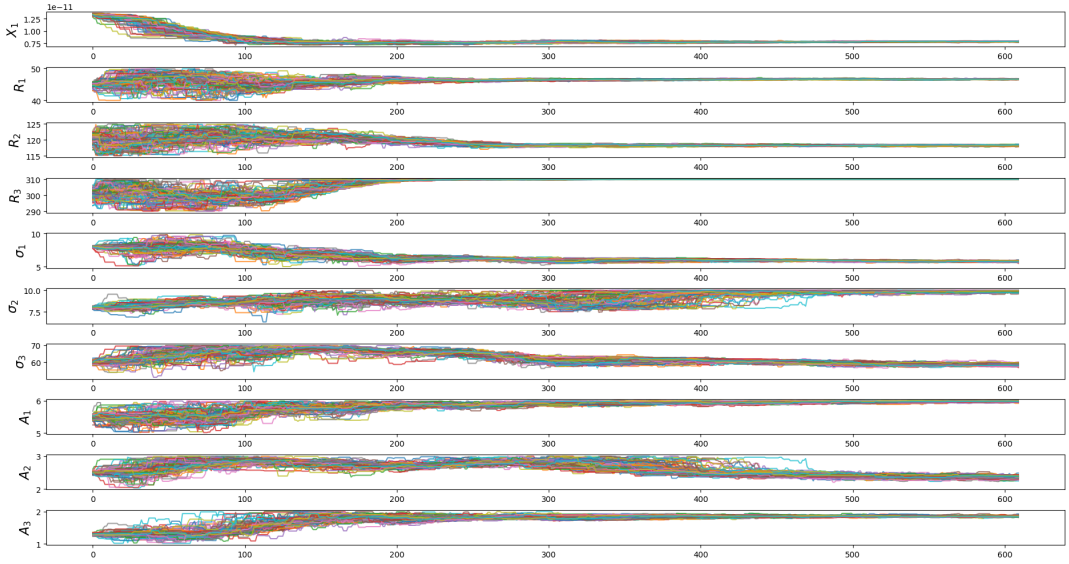

Figure 4.6: The figure shows the fitting results obtained for the HCN molecule, modeling the bright substructures of the disk. The figure demonstrates how the walkers evolve over the iterations that emcee uses to explore the parameter space, specifically for the parameters X_1, R_n, σ_n, and A_n. A total of 100 walkers were used in 610 iterations. The numerical results and uncertainties can be seen in table 4.3.

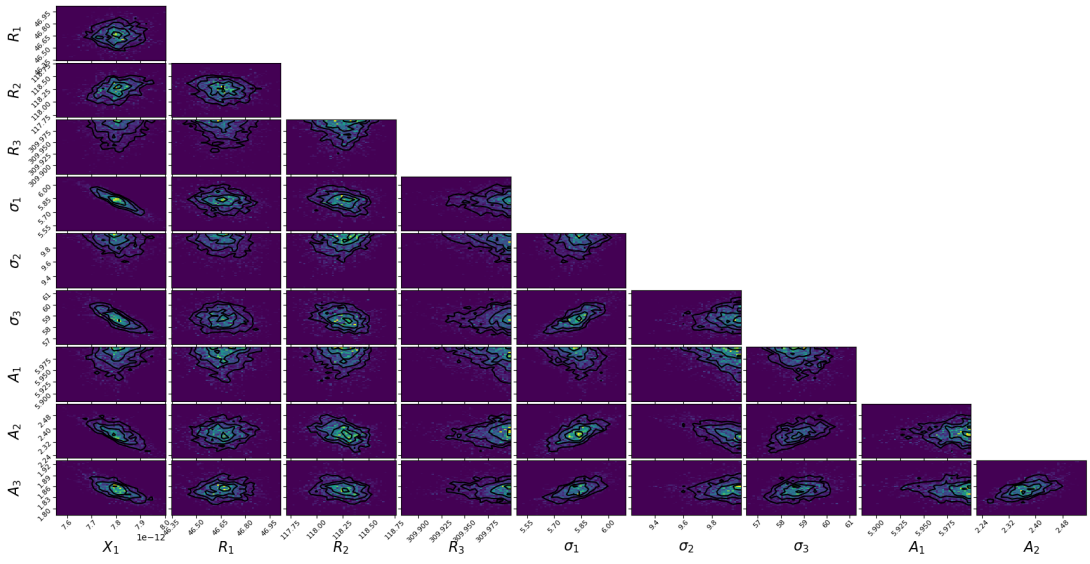

Figure 4.7: The figure shows the corner plots and the correlation between the different fitted parameters. In this case, for the HCN molecule, 10 parameters were fitted, to represent the 3 bright rings as substructures of the disk.

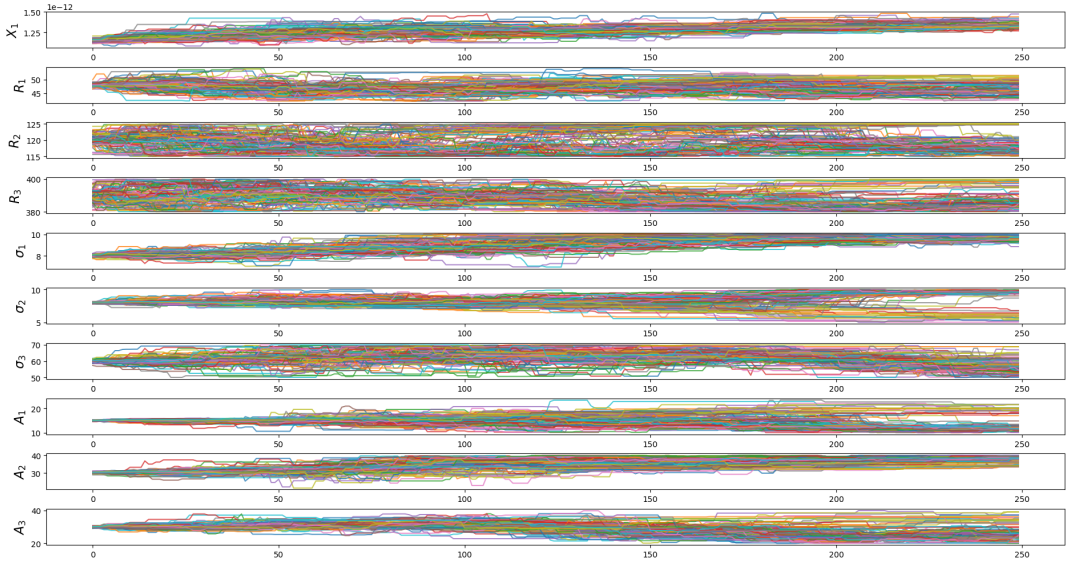

Figure 4.8: The figure shows the fitting results obtained for the C_2H molecule, modeling the bright substructures of the disk. The figure demonstrates how the walkers evolve over the iterations that emcee uses to explore the parameter space, specifically for the parameters X_1, R_n, σ_n, and A_n. A total of 100 walkers were used in 250 iterations. The numerical results and uncertainties can be seen in table 4.3.

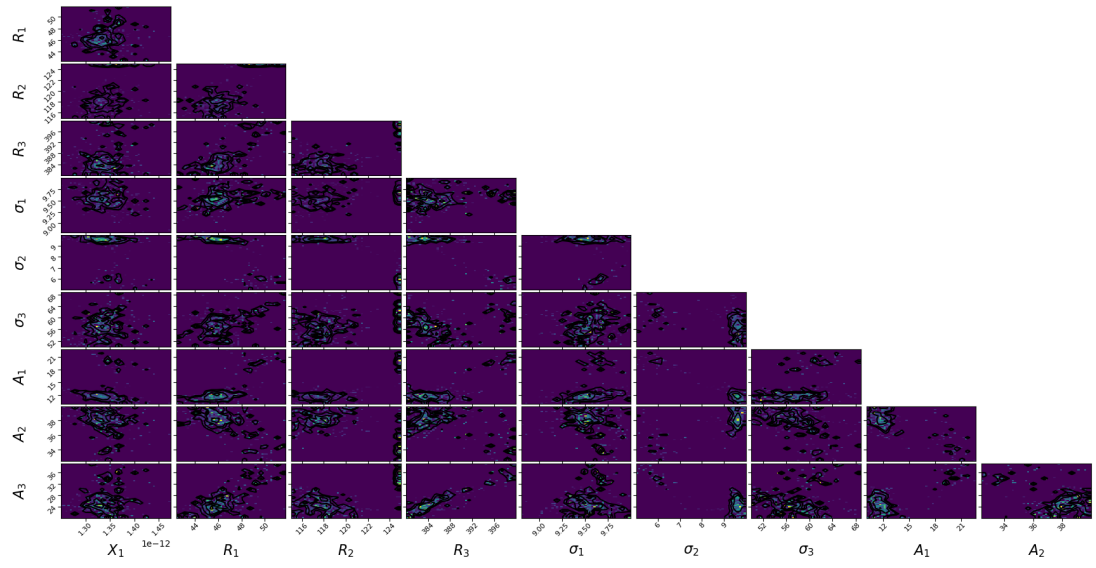

Figure 4.9: The figure shows the corner plots and the correlation between the different fitted parameters. In this case, for the C_2H molecule, 10 parameters were fitted, to represent the 3 bright rings as substructures of the disk.

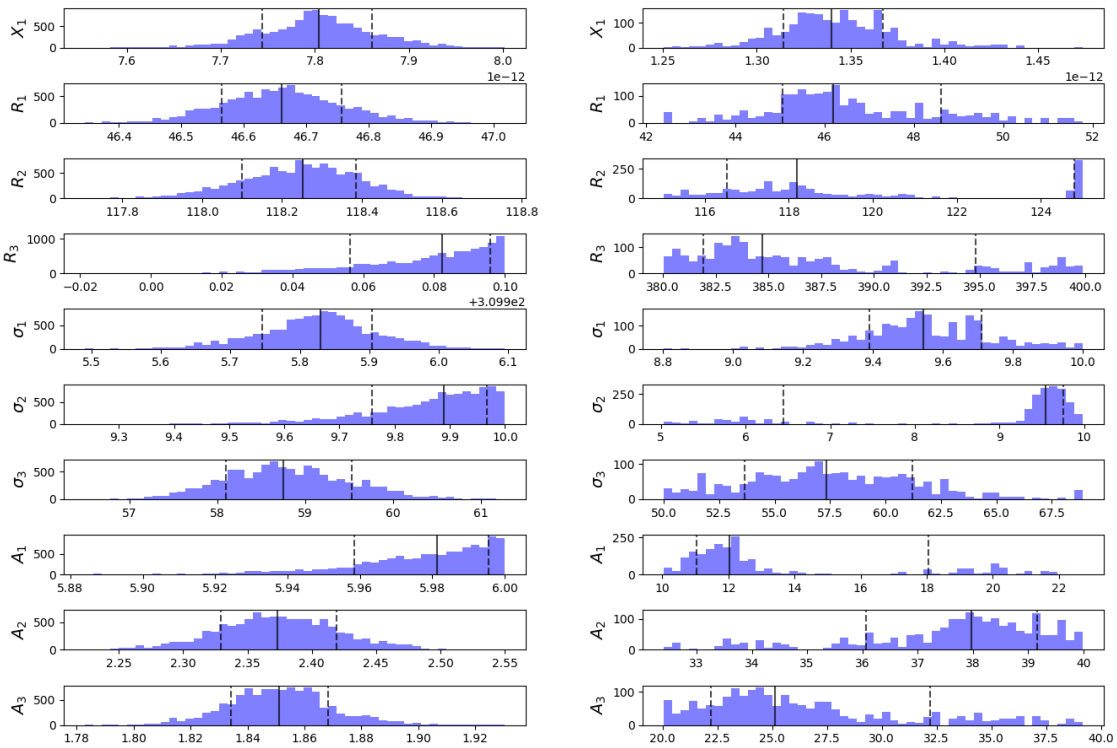

Figure 4.10: The figure shows the histograms corresponding to the marginal distributions of each of the parameters in the corner plots analysis, in this case for HCN (left) and C_2H (right). Each histogram illustrates how the values of a specific parameter are distributed while keeping the other parameters fixed. For both molecules, the numerical results corresponding to the 50th percentile (solid black line), which is the median of the data, can be seen in Table 4.3 with their respective uncertainties. The dashed black lines correspond to the 16th and 84th quintiles respectively

From the values obtained from the MCMC fit in the parameterization of the general structure plus the substructures, synthetic images have been generated using RADMC-3D, which we compare with observational data in band 6 for the HCN and C_2H molecules. Figures 4.11 and 4.12 show the velocity channels comparing the observational data with the generated synthetic models, in addition to calculating the difference (residuals) between the model and the observation. Finally, the deprojected profiles of the synthetic models were generated, comparing them with those of the observations, which can be seen in figure 4.10.

Species	$X_{1}{}^{+\delta Xu}_{-\delta Xl}$	$R_{n}{}^{+\delta Ru}_{-\delta Rl}$	$\sigma_{n}{}^{+\delta \sigma u}_{-\delta \sigma l}$	$A_{n}{}^{+\delta Au}_{-\delta Al}$
HCN	$7.80\text{e-}12^{+0.05}_{-0.06}$	$46.7^{+0.1}_{-0.1}$ $118.3^{+0.1}_{-0.2}$ $309.98^{+0.01}_{-0.03}$	$5.84^{+0.08}_{-0.08}$ $9.89^{+0.09}_{-0.13}$ $58.7^{+0.8}_{-0.7}$	$5.98^{+0.01}_{-0.02}$ $2.38^{+0.05}_{-0.04}$ $1.86^{+0.02}_{-0.02}$
C_2H	$1.34\text{e-}12^{+0.03}_{-0.03}$	46^{+2}_{-1} 118^{+7}_{-2} 385^{+10}_{-3}	$9.5^{+0.2}_{-0.2}$ $9.5^{+0.2}_{-3.0}$ 57^{+4}_{-4}	12^{+6}_{-1} 38^{+1}_{-2} 25^{+7}_{-3}

Tabla 4.3: The table shows the values and uncertainties obtained after fitting the parameters for the entire structure of HD 163296 for HCN and C_2H molecules. The parameters are the relative abundance X_1, central position of the rings R_n, ring width σ_n, and the scale factor of the ring amplitude A_n.

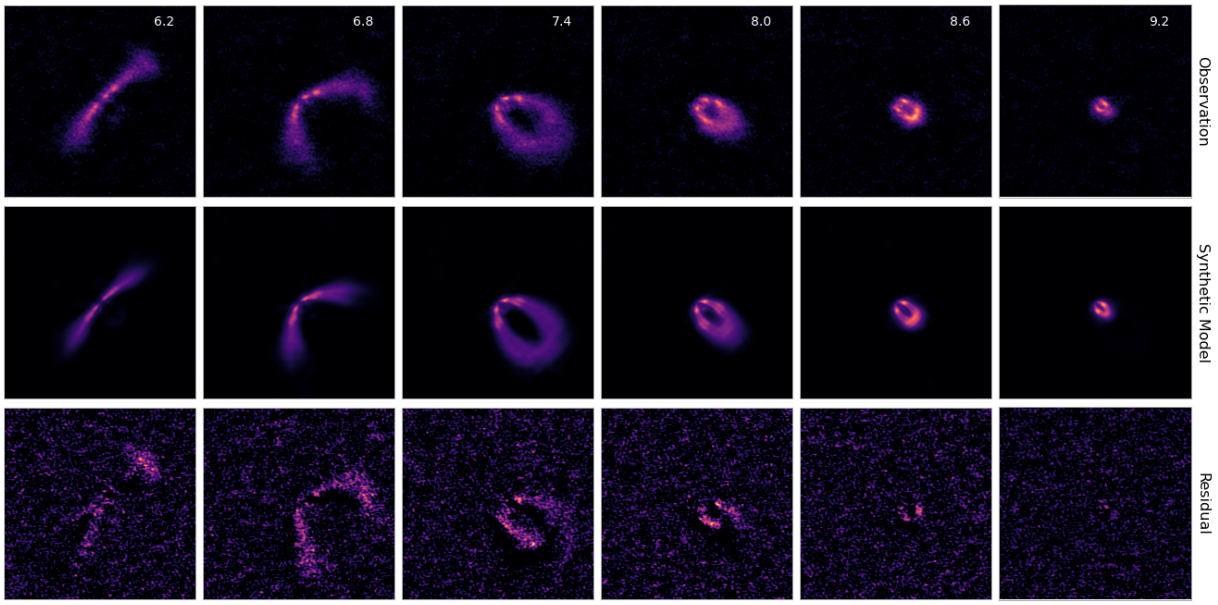

Figure 4.11: The figure displays the velocity channel map for HCN. The top row shows the observation channels for Band 6 (J=3-2), with its respective speed channel (in units Km/s). The second row displays the channel map resulting from the synthetic model using the values obtained after the emcee fit for the complete disk structure (4.3). The third row presents the residual channels concerning the observation with the synthetic model. The range values for the residual detection is 6.8σ to 4.2σ.

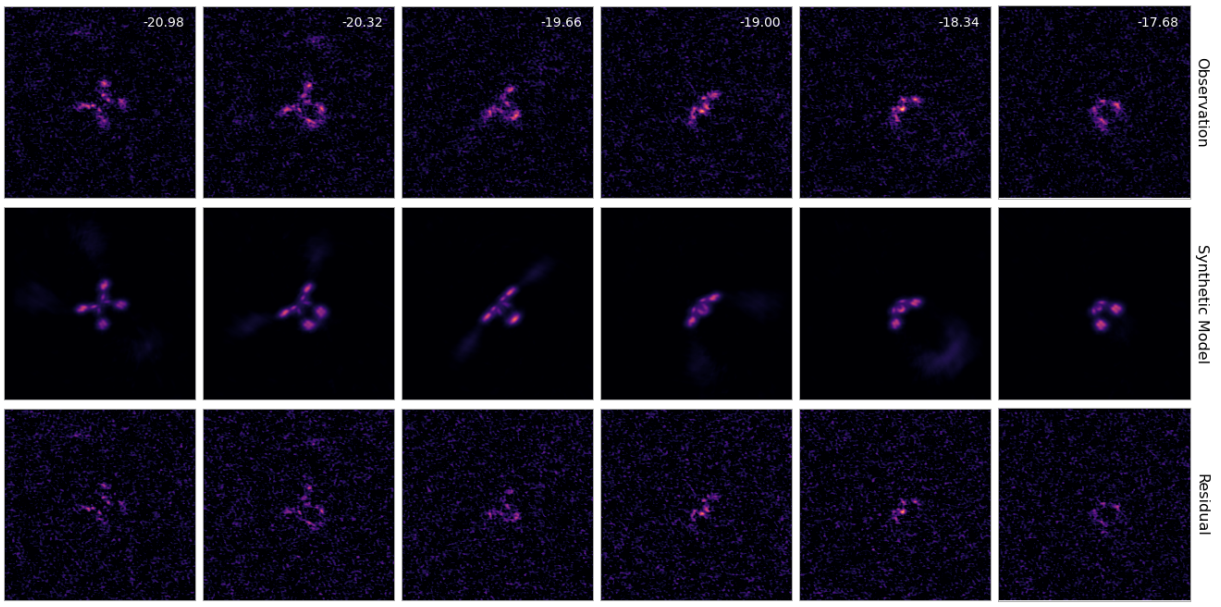

Figure 4.12: The figure displays the velocity channel map for C_2H. The top row shows the observation channels for Band 6 ($J = 3-2$). The second row displays the channel map resulting from the synthetic model using the values obtained after the emcee fit for the complete disk structure (4.3). The third row presents the residual channels concerning the observation with the synthetic model. The range values for the residual detection is 8.6σ to 5.5σ.

From the best values obtained by the fit, we were able to reconstruct a radial profile of the complete structure of the HD 163296 disk. The modeled substructures were three for both molecules and were compared with observations in band 6. The deprojected profiles can be seen in Figure 4.13. The intensities of HCN tend to be more abundant in the area closest to the star, while C_2H is not very abundant in the inner disk of HD 163296. Overall, HCN and C_2H show similar radial distributions where two of the bright rings have quite a good correlation in the range of 46 to 150 au. The abundance of C_2H begins to drop faster, after the second bright ring, in comparison to HCN, beyond 150 au.

Finally, Figure 4.14 displays the profiles of the relative abundances for HCN and C_2H constructed from the parameters of the best fit (Table 4.3). The distribution of gas abundance in the HD 163296 disk was obtained using a power law for the general structure and Gaussian functions to model the bright rings.

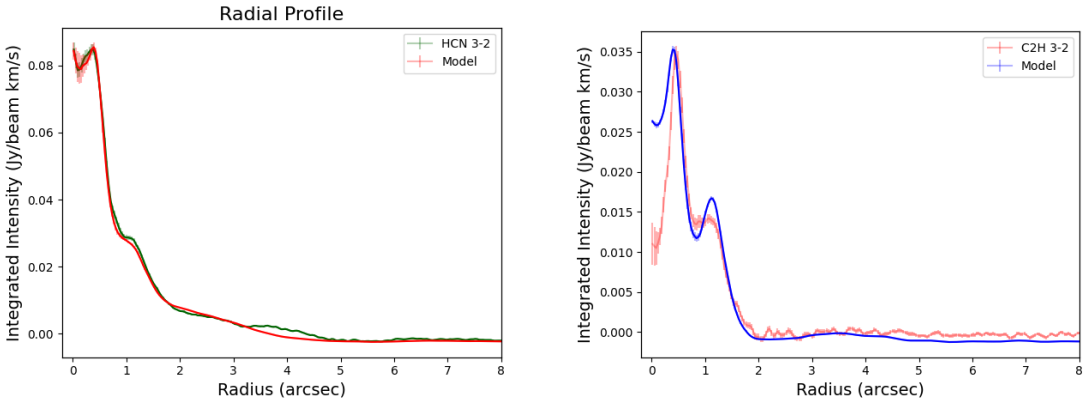

Figure 4.13: The figure shows the radial profiles of the zeroth moment of the observation data in Band 6 for the HCN and C_2H molecules and compares with the synthetic models. The horizontal axis represents the distance from the center of the HD 163296 disk (”), and the vertical axis shows the integrated intensity (Jy/beam km/s). The synthetic models were generated using the values from Table 4.3, using the parameters to simulate the gas substructures observed in HCN and C_2H.

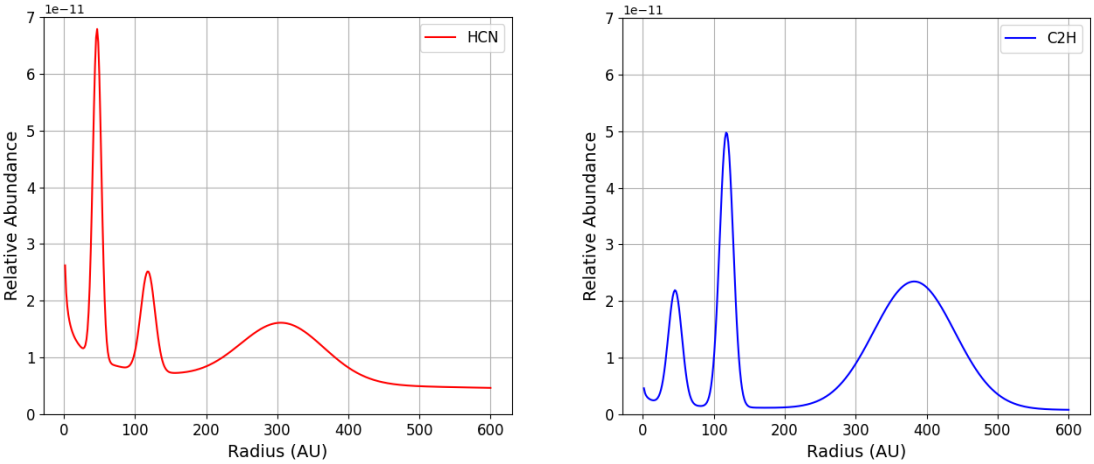

Figure 4.14: The figure shows the relative abundance distribution for the HCN and C_2H molecules. The horizontal axis represents the distance from the center of the HD 163296 disk (au), and the vertical axis shows the relative abundance.

Chapter 5

Discussions

This research focused on modeling the structure and substructures of the molecular gas in the protoplanetary disk HD 163296. Interferometric data taken by the MAPS collaboration were used. A rigorous methodology was implemented to estimate the best parameters that reproduced the observed line emission for HCN and C_2H. This included multiple tests to fine-tune the parameters of the HCN and C_2H molecules in the disk. The results showed significant adjustments in the model parameters, such as the relative abundance of molecules and the features of the bright rings. This adjustment was essential for a better understanding of the composition and structure of the protoplanetary disk. This chapter will discuss the main results obtained in this study and compare the findings with recent studies.

5.1 Vertical distribution of the small molecules

The MAPS collaboration presents a detailed analysis of the vertical distribution of molecules and their emitting surfaces in high angular resolution observations of five protoplanetary disks (Law et al. (2021c)). The emission heights of C_2H and HCN were estimated, and it is suggested that the emission comes from a height $Z/R \sim 0.1$ or even lower, relatively close to the midplane of the planet-forming disk. Our models and results have shown that the lower height for the HCN molecule comes from a $Z/R\ low = 0.11$, which corresponds to the best fit based on the parameter calculation resulting from the emcee. On the other hand, the C_2H molecule shows an even lower emission height of $Z/R\ low = 0.067$. The emission heights that we estimate in this research are consistent with the height estimates made by the MAPS team in Law et al. (2021c). With observations at only two frequencies, it is assumed that the distribution of the molecules' emission follows a trend that can be extrapolated to other frequencies. The accuracy in estimating $Z/R\ low$ would increase with additional data across a broader range of frequencies, allowing for a more precise characterization of how the emission varies with height in the disk. With only two data points, caution must be exercised in extrapolation, as the inferred trends

might not capture the full physical complexity of the disk.

Additionally, Law et al. (2021b) and Law et al. (2021c) suggest that HD 163296 is the only source in the MAPS collaboration where vertical substructures are visible for the HCN and C_2H lines. Our modeling on the substructures suggests that these substructures for both molecules correspond to 3 bright rings located at 46.7 au and 118.3 au in the inner part of the disk (< 200 au) and at 309.98 au in the outer disk for the HCN molecule. For C_2H, the bright substructures are found at 48, 120, and 385 au, which are consistent with those determined in the literature Law et al. (2021b) and Law et al. (2021c).

5.2 Comparing HCN and C_2H with the continuum emission

If HCN and C_2H are produced primarily through UV radiation-driven chemistry, enhanced abundance could be expected in the regions with dust gaps. In these dust-depleted zones, UV photons could penetrate more deeply, potentially leading to more effective formation of C_2H and HCN. Nonetheless, the extent of UV photon penetration is also influenced by the source's geometric configuration.

The deprojected profiles of HD 163296 (see figure 5.1) show a notable decrease in the intensity of the HCN and C_2H molecules after the first bright ring beyond 50 au. Even before reaching the new peak of the second bright ring (∼118 au), the abundance decreases a bit more, which coincides with one of the dust gaps (CO) near 83 au, where the location of a planet has been proposed (Teague et al. (2018b)). The peak abundance of C_2H and HCN seen towards the first bright ring of HD 163296 coincides with the location of the innermost dust gaps (∼47 au), though it is broader in comparison to the dust gaps. The rich abundance of both molecules in the inner disk of HD 163296 (<150 au) could suggest that organic chemistry is much richer in the inner disk or that in the outer disk the molecular emission remains hidden in the ice. The second bright ring of C_2H and HCN, at ∼118 au, does not spatially coincide with any of the dust gaps, revealing that there is no universal connection between dust depletion and the formation of C_2H or HCN.

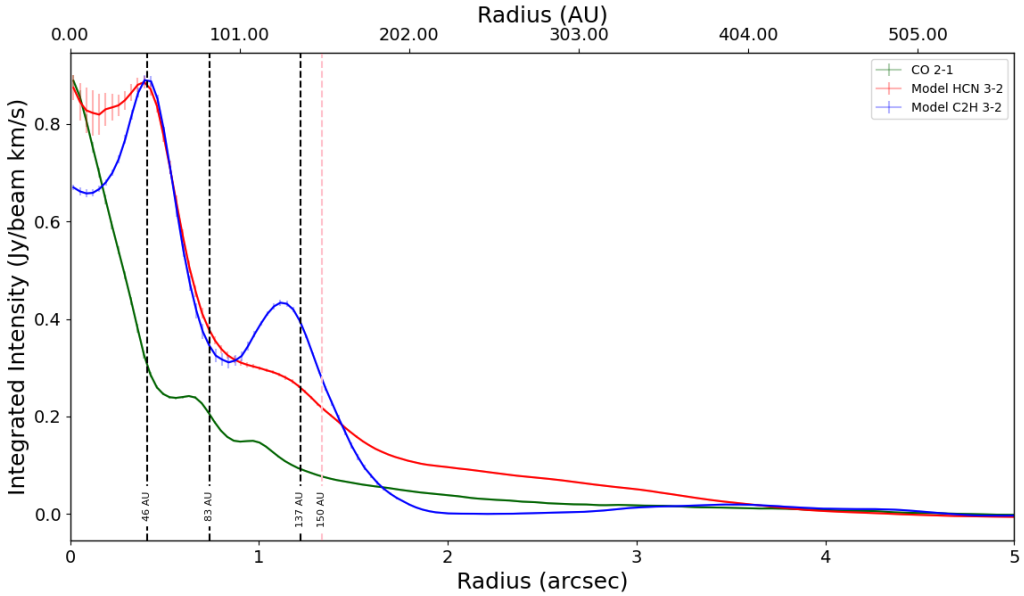

Figure 5.1: The figure shows the comparison of the deprojected profiles of the synthetic models for HCN and C_2H with observations of the dust (CO 2-1, 220 Ghz) in the disk HD 163266. The vertical dashed lines correspond to the location of the millimetric dust gaps and where has proposed the location of planets formed in the disk. The vertical pink dashed line at 150 au is used as a reference to the beginning of the outer disk of HD 163296.

Within a distance of 150 au, see figure 5.1, a significant spatial overlap is observed between dust and chemical substructures, mainly the third HCN and C_2H gap begins to be seen and the dust decreases considerably. However, in the outer regions of the disks, these overlaps are less frequent. This indicates that in the inner areas of the disk, the midplane that emits dust and the warm molecular layers are interconnected, but this connection diminishes progressively in the outer and larger radii of the disk. The most external bright rings in our models in C_2H 3-2 and HCN 3-2, occur at very extended radii, $\sim$309 and $\sim$385 au, and there is no correlation with CO as no CO substructures are observed in the observations taken by MAPS Law et al. (2021b).

The Figure 5.1 shows that there is not much correlation between dust and the chemical substructures of HCN and C_2H. This could be due to the emissions of HCN and C_2H arising from higher layers of the disk ($Z/R = 0.68$-0.11), which are not always affected by the millimeter-scale dust substructure that traces the midplane.

5.3 Formation pathways in HD 163296

If the formation of HCN and C_2H is governed by photochemical processes, an enhanced emission could be anticipated in the outer regions of the disk. This is where a decrease in gas density could enable deeper penetration of UV photons into the disk. Weak emission is detected at large radii, far beyond the millimeter dust edge in HD 163296. As seen in Figures 4.13, the faintest bright rings reach outer radii of 309 and 385 au for HCN and C_2H, respectively.

The chemical explanation to justify the increase in abundance of some species requires that the CO gas is sufficiently depleted at the locations of the substructures (Law et al. (2021c)). If these features have their origin in chemistry, the depletion of CO in the gaseous phase should lead to higher C/O ratios, meaning that Carbon (C) becomes more abundant and there is an increase in the column density of molecules like C_2H, which forms from free C in the gaseous phase (Alarcón et al. (2021)). The substructures in HD 163296 are associated with the depletion of CO density (Zhang et al. (2021)) and an increase in C_2H (Guzmán et al. (2021b)). This suggests that the chemical conversion of CO into other species may provide, at best, a partial explanation for the observed vertical substructures and the increase in the abundance of C_2H. In Bosman et al. (2021) discovered that elevated C/O ratios are needed to explain the observed abundances of C_2H for HD 163296. Therefore, C_2H is very sensitive to the C/O abundance ratio in the gaseous phase in the disk's atmosphere (Bergin et al. (2016b)). Moreover, the formation of cyanide generally depends on the availability of free carbon (Le Gal et al. (2019)), thus a high C/O ratio allows for abundant formation of HCN. The relationship between the abundance of CN and HCN has been studied for all MAPS sources in Bergner et al. (2021b), which shows that the local column densities of CN and HCN within different radial bins have a positive trend with each other.

5.4 Limitations and Future Directions

Based on the results obtained from RADMC-3D to model the protoplanetary disk HD 163296, coupled with the implementation of emcee for MCMC analysis, here are some potential limitations in the methodology:

- The results of RADMC-3D are heavily dependent on the initial parameters and assumptions made in the model setup. Extrapolation based on limited data can lead to incorrect interpretations if the model does not accurately capture the physical complexity of the disk.
- While emcee provides a robust way to explore the parameter space, the resulting uncertainties can be significant, especially if the Markov chain has not fully converged or if the underlying model is an excessive simplification of reality.

- RADMC-3D, especially when combined with MCMC analysis, can be computationally intensive, which limits the amount of parameter exploration or the depth of analysis in some cases, and also requires a considerable amount of computing time in many instances.

Some suggestions for future projects or research directions:

- Expanding the exploration of parameter spaces in MCMC simulations could help to better understand uncertainties and improve correlations between model parameters. This might involve using emcee to simulate a wider range of physical and chemical conditions in the disk.
- Integrating more complex models that include more complex physical processes, such as the determination of the molecular emission height (Z/R), which tends to be more complex than that used in this research, could provide a deeper understanding of the disk's structure and emission.
- Applying similar techniques to other protoplanetary systems and comparing the results can help identify common trends or significant differences in the formation and evolution of disks, in both low and high-mass stars. Additionally, integrating the methodology for the characterization of the substructures of other species, like H_2CO, within the HD 163292 disk.

Chapter 6

Conclusions

We present an analysis of the vertical emission of small molecules, HCN and C_2H, and their emitting surfaces in high angular resolution observations of the protoplanetary disk HD 163296 from MAPS. Additionally, we present the modeling and characterization of the radial substructures of molecular gas around the disk. The main conclusions are as follows:

- A rigorous methodology was implemented to estimate the parameters of the disk, both its general structure and its bright rings, using initial models and then refining them with emcee. This included multiple tests to fine-tune the parameters of the HCN and C_2H molecules in the disk.

- Through the analysis of the vertical emission of the molecules HCN and C_2H, we tested three models for HCN to determine the height from which the molecular emission originates in the general structure of the disk. The best model determined that the vertical emission closest to the midplane comes from a height of $Z/R = 0.11$ for HCN. For C_2H, testing with the best model indicated that the emission comes from lower layers at $Z/R = 0.068$.

- The substructures of the gas were modeled through Gaussian functions, of which 3 bright rings have been characterized for each molecule. For HCN, the inner ring is located at 46.7 au from the central star, with a width of 5.84 au and a scale factor relative to the abundance of 5.98. The second ring is positioned at 118.3 au, with a width of 9.89 au and a scale factor of 2.38. The third ring is at 309.98 au with a width of 58.7 au and a scale factor of 1.86 au. For C_2H, the inner ring is located at 46 au from the central star, with a width of 9.5 au and a scale factor relative to the abundance of 12. The second ring is at 118 au, with a width of 9.5 au and a scale factor of 38. The third ring is at 385 au with a width of 57 au and a scale factor of 25 au.

- The comparison of synthetic models with continuum observations has shown that in general, the substructures of gas and dust are not correlated. The gap at 83 au,

where a forming planet has been proposed, could be the only correlation between dust and molecular gas.

- The outermost rings in the HCN 3-2 and C_2H 3-2 models occur at very extended radii, approximately 309 and 385 au respectively, and do not show correlation with CO, as no CO substructures are observed in the MAPS observations. Even the radial profiles of HCN suggest that there could be another ring close to 400 au.

- The relative abundance distribution for HCN shows 3 peaks of emission, each positioned at one of the bright rings. The peak of abundance occurs at the first ring (46.7 au) with a value of $\sim 6.8 \times 10^{-11}$, the second peak (118.3 au) reaches a value of $\sim 2.5 \times 10^{-11}$, and the third peak (309.98 au) reaches a value of $\sim 1.7 \times 10^{-11}$, showing a decreasing trend as we move away from the star. For C_2H, the abundance distribution does not follow a decreasing trend, like HCN, as the peak of abundance occurs at the second bright ring (118 au) reaching a value of $\sim 5.0 \times 10^{-11}$. In the other two rings, the abundance is relatively similar, reaching values of $\sim 2.2 \times 10^{-11}$ and $\sim 2.4 \times 10^{-11}$ for the rings located at 46 and 385 au respectively.

- We hope that this model will be useful for interpreting astronomical observations of protoplanetary disks and understanding the distribution of material that could lead to planet formation.

Appendix A

Interferometric Theory

Interferometry and its beginnings date back to around 1868 at the Marseille Observatory in France. During those years, the need to establish a connection between observations and the phenomenon of light interference arose. This concept was introduced in the work of Fizeau (Fizeau (1867)), who proposed placing a screen with two holes in front of the largest telescope of that time to gather new data on the angular diameters of stars (Quirrenbach (2009)). Later on, the mathematical formalism of interferometric theory was developed by Michelson, who is considered the inventor of interferometry (Michelson (1920)). This marked a turning point in observation techniques. In the following sections, basic concepts of this technique will be presented to familiarize the reader with the interferometric observation techniques implemented in the development of this thesis.

A.1 Angular Resolution

One of the advantages of Interferometry is its capability to achieve high resolution, enabling the capture of fine details of distant celestial objects and providing insights into the underlying physical processes. However, achieving resolutions finer than arc seconds is limited by the impracticality of constructing large telescopes due to their inevitable deformation caused by their weight. An example of this situation was the collapse of the Arecibo radio telescope located in Puerto Rico, a 305-meter parabolic antenna weighing 900 tons, which collapsed on December 1, 2020, after approximately 60 years of operation.

Therefore, the concept of simulating a single telescope by constructing an array of antennas that share the same properties, all positioned at the same geographic location, allows for achieving those levels of resolution. This technique is known as Interferometry, and the diameter of this simulated single element is defined by the following equation:

$$D = [N(N-1)]^{0.25} d \ , \tag{A.1}$$

where D is the simulated diameter of the interferometer, N is the number of antennas

and d is the diameter of each one. However, the resolution capacity of an interferometer is limited by the maximum distance between two antennas, which is known as the baseline. Therefore, the detail of the observation or the angular resolution Θ of the simulated telescope satisfies the following expression:

$$\Theta \propto \frac{\lambda}{B} \, , \tag{A.2}$$

where the parameter B corresponds to the baseline and λ is the wavelength of the observation. With the angular resolution Θ in units of arcsec. This expression shows the inverse relationship between the observation detail and the separation of two antennas, the greater the distance between the two antennas, the lower the value of the parameter *Theta*, which translates into a better resolution and greater detail obtained from the observed source. The baseline is translated as two points (real and imaginary) in an imaginary plane denoted by *plane-uv*. The coverage of said plane is crucial according to the actual structure recovered from the object in question, because the more populated it is, the better the signal response. However, covering it homogeneously is something impossible, if the rotation of the Earth is not considered.

If the elements of an interferometer have the ability to move, it is possible to define different configurations of itself. Therefore, it is a technique with greater flexibility in aspects of angular resolution. The angular resolution capacity depends on the maximum distance between baselines, as defined in equation A.2. It is generally classified into two main types of configurations: compact and extended. The more extended distributions define a better angular resolution, being sensitive to small spatial scales. On the other hand, compact distributions allow to study objects of large spatial scale.

A.2 Visibility

In practical terms, in interferometry, all the physical information of a source to be analyzed is contained in a single quantity defined as Visibility. For a simple array of two antennas, the visibility can be represented as shown in Figure A.1.

The mathematical deductions presented in this sub-section are formulated through the book *Tools of Radio Astronomy, 5th edition* by Wilson et al. (2012) and the notes of the *Essential Radio Astronomy* created by Condon & Ransom (2016).

In the context of a simple interferometer (A.1), the response for the first and second antennas is written as:

$$V_1 = V \cos[\omega(t - \tau_g)] \tag{A.3}$$

and for the second antenna as

$$V_2 = V\cos(\omega t)\ , \tag{A.4}$$

where t is the time, $\omega = 2\pi\nu$ is the oscillation frequency and τ_g corresponds to the time delay, generated by the difference in the arrival of the signal between antennas and is written as:

$$\tau_g = \vec{B}\cdot\hat{s}/c\ , \tag{A.5}$$

where $\vec{B}$ is the baseline vector, $\hat{s}$ is the direction of the unit vector for the position S of the source, and c is the speed of light.

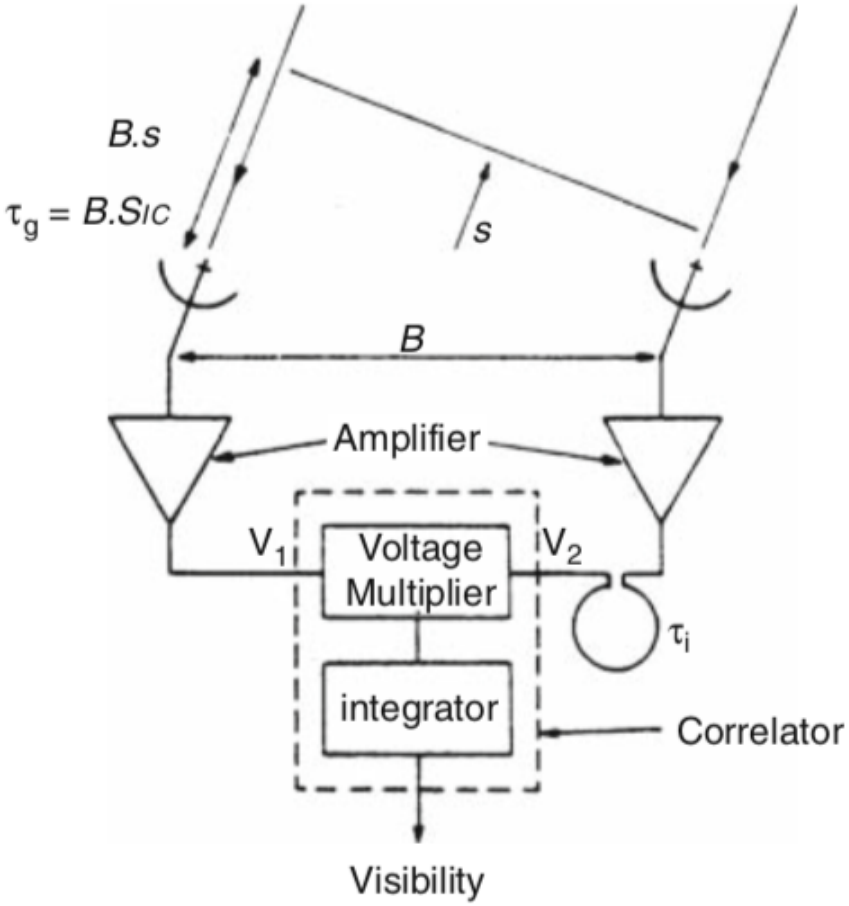

Figure A.1: Diagram of a simple interferometer with two antennas. The separation between the antennas is defined as the baseline and is denoted in the figure by the vector $\vec{B}$. The signal wavefront of the observed object is represented by the unit vector $\hat{s}$. The signal received by each antenna (V_1 and V_2) presents a difference, which is compensated through the parameter τ_g. The signals are taken to the correlator, to finally process all the information from the source, in the quantity called *Visibility*, which contains information about the amplitude and phase of the object. The parameter τ_i represents the instrumental delay. reference: Wilson et al. (2012).

Both signals are derived from the correlator, which is in charge of first generating a multiplication between them, to then be averaged over a sufficiently long time, that is, $t \gg (2\omega)^{-1}$, and thus obtain a únique answer R that satisfies the following expression:

$$R = < V_1 V_2 > = \frac{V^2}{2} \cos(\omega \tau_g) \ . \tag{A.6}$$

The response R of the correlator presents a sinusoidal variation as the interferometer moves due to the rotation of the Earth, so the source changes direction. These sinusoidal

variations are known as *fringes* ϕ, and they satisfy the following relationship:

$$\phi = \omega\tau_g = \frac{\omega}{c}\, b\cos(\theta)\ , \tag{A.7}$$

where the parameter b is the magnitude of the vector baseline $\vec{B}$ and θ is the ángle between the unit vector $\hat{s}$ and the vector $\vec{B}$.

For the case of an extended source with a brightness distribution in the sky $I_\nu(\hat{s})$ (see the figure A.2), the response of the interferometer composed of only two elements, is obtained analogously, by extending the previous analysis in a sum of point sources, in such a way that the following relationship is satisfied:

$$R = \int I_\nu(\hat{s})\cos\left(2\pi\nu\vec{B}\cdot\hat{s}/c\right)\, d\Omega = \int I_\nu(\hat{s})\cos\left(2\pi\vec{B}\cdot\hat{s}/\lambda\right)\, d\Omega\ , \tag{A.8}$$

The λ parameter is the wavelength of the observation.

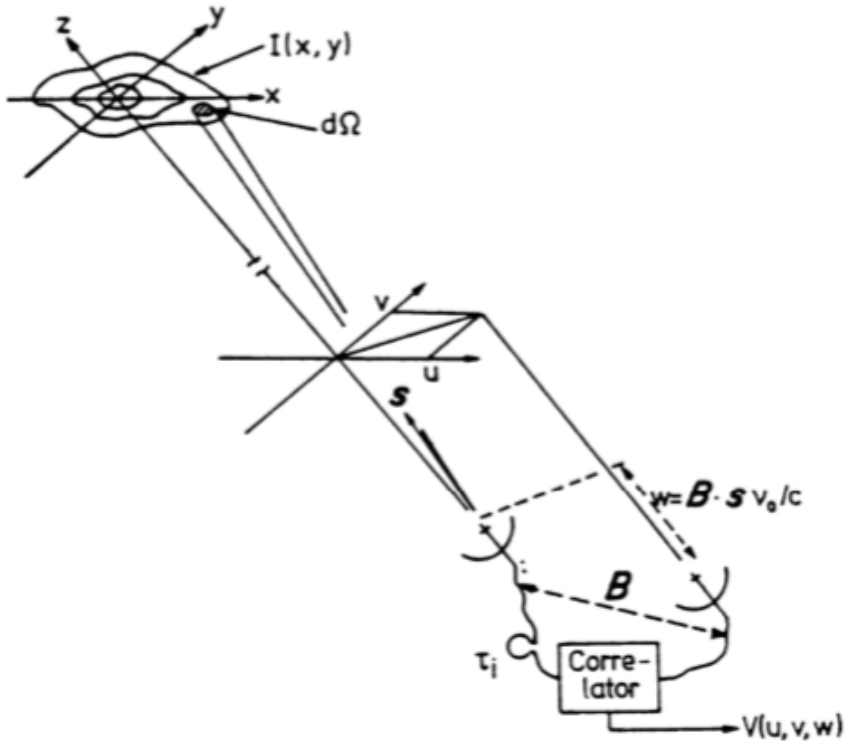

Figure A.2: The geometry of observation for a simple interferometer. The upper part of the figure shows the brightness distribution I_ν for an extended source, and the representation of the solid ángle $d\Omega$. In the middle of the figure, the projection of the baselines in the uv-plane is shown. The lower part of the figure shows the vector $\vec{B}$, corresponding to the distance between two antennas, the geometric delays τ_g, and instrumental τ_i. All information from the source is brought to the correlator and processed to get Visibility ($\mathcal{V}_\nu$). reference: Wilson et al. (2012).

However, the response A.8 is sensitive to only a part of the entire brightness distribution $I_\nu(\hat{s})$, which can be broken down into a sum of even and odd elements: $I = I_{even} + I_{odd}$ and from now on, the response A.8 is denoted by $R_{even} = R_c$. With which the detection of the other component, associated with the odd factor, is attributed to a second correlator with a phase delay of 90^{o}. The antenna response for said correlator is written as:

$$R_{impar} = \int I_\nu(\hat{s}) \sin\left(2\pi\nu\vec{B}\cdot\hat{s}/c\right)\, d\Omega = \int I_\nu(\hat{s}) \sin\left(2\pi\vec{B}\cdot\hat{s}/\lambda\right)\, d\Omega = R_s\ . \tag{A.9}$$

Mixing the equations A.8 and A.9 gives a new concept called complex correlator. A quantity is introduced by using the properties of Euler's equation ($e^{i\phi} = \cos(\phi) + i\sin(\phi)$) on the response of both antennas as follows:

$$\mathcal{V}_\nu = R_c - iR_s = \mathcal{A}e^{i\phi} \tag{A.10}$$

where $\mathcal{V}_\nu$ is called the Complex Visibility, the parameter $\mathcal{A}$ corresponds to the amplitude and ϕ the phase of the Visibility. The definitions for amplitude $\mathcal{A}$ and phase ϕ are respectively:

$$\mathcal{A} = \sqrt{R_c^2 + R_s^2} \tag{A.11}$$

and,

$$\phi = \tan^{-1}(R_s/R_c) \ . \tag{A.12}$$

In this way, the answer for the case of a simplistic interferometer of an extended source, with a brightness distribution in the sky $I_\nu(\hat{s})$, through 'is from the processing of the *complex correlator* is, the *Complex Visibility*:

$$\mathcal{V}_\nu = \int I_\nu(\hat{s}) \exp\left(\frac{-i2\pi\vec{B}\cdot\hat{s}}{\lambda}\right) d\Omega \ . \tag{A.13}$$

For simplicity, it is necessary to make a change of coordinates for the unit position vector $\hat{s}$. This vector describes the position in the sky of the object, in Right Ascension (R.A) and Declination (Dec) coordinates. But, it is necessary to take these coordinates to the uv-plane, through the concepts of spatial frequencies $u \equiv \frac{B_x}{\lambda}$ and $v \equiv \frac{B_y}{\lambda}$, where the Parameters B_x and B_y correspond to the modules of the baseline vector in the East-West and North-South directions, respectively. Finally, complex visibility can be written as:

$$\mathcal{V}_\nu(\alpha,\beta) = \int d\alpha \int d\beta I(\alpha,\beta) e^{-i2\pi(u\alpha+v\beta)} \tag{A.14}$$

where the distribution of brightness in the sky $I(\alpha,\beta)$ is presented in coordinates of R.A and Dec, denoted by α and β, respectively.

A.3 Van Cittert-Zernike theorem

The Van Cittert-Zernike theorem refers to the principle of Interferometry, which states that the measurement from an interferometer does not generate a synthesized image; instead, its response is the Fourier transform $\mathcal{FT}()$ of the intensity from the observed source. In other words, it is the Visibility $\mathcal{V}_\nu$ as seen in the previous section.

The complete formalism of the Van Cittert-Zernike theorem is addressed in Chapter 15 of the book Interferometry and Synthesis in Radio Astronomy, 3rd Edition by Thompson et al. (2017). However, the current subsection provides a concise explanation of the theorem's definition.

Mathematically, the two-dimensional Fourier transform for an arbitrary complex function $f(x,y)$ is defined through the following expression:

$$\mathcal{FT}(u,v) \equiv \int\int_{-\infty}^{+\infty} f(x,y)e^{-i2\pi(ux+vy)}\, dxdy \tag{A.15}$$

Where the parameters u and v correspond to spatial frequencies (not necessarily those described earlier) in the x and y directions, respectively.

Now, comparing the previous equation A.15 with the definition for the interferometric quantity called Complex Visibility represented in equation (A.14), we obtain the following:

$$\mathcal{V}_\nu(\alpha,\beta) = \mathcal{FT}\left[I(\alpha,\beta)\right] \ , \tag{A.16}$$

The above is the response of the interferometer and thus the new definition of Complex Visibility, according to the Van Cittert-Zernike theorem in terms of the Fourier transform. Therefore, to obtain the image of the brightness distribution I_ν of an astronomical source, it is necessary to apply the inverse Fourier transform $\mathcal{FT}()^{-1}$ to equation A.16. This relationship is known as the principle of Interferometry.

A.4 IR and (Sub)millimeter astronomy

Radio astronomy was born around the early 20th century when a Bell Labs employee in New Jersey named Karl G. Jansky unraveled a bigger mystery of his time — the interference plaguing radio communications across the Atlantic. He discovers that this interference emanates from the center of the Milky Way galaxy. His findings were published in 1933 under the title Radio Waves from Outside the Solar System (Jansky, 1933), marking the foundational moments of radio astronomy.

This field of Astronomy is devoted to studying objects at long wavelengths (λ), specifically on the order of centimeters (cm), millimeters (mm), and submillimeter ($submm$). At these wavelengths, various types of sources become visible that are typically invisible to our eyes, for instance, gas and molecular clouds, as well as plasma ejections from the centers of supermassive black holes and observations of the center of the Milky Way. Recently, thanks to this technique, high-impact studies have been published, enabling to observation of the atmosphere of the Red Giant Antares and Betelgeuse (O'Gorman et al., 2020), and even providing the first image of a black hole in the galaxy M87 through the Event Horizon Telescope (EHT) (Event Horizon Telescope Collaboration et al., 2019).

A.4.1 Flux in units of Jansky.

The following deduction and its general concepts are drawn from chapter one of the book Tools of Radio Astronomy by Wilson et al. (2012).

We begin by assuming that radiation travels in a straight line due to the scale of the system itself compared to the observed wavelength, as illustrated in figure A.3.

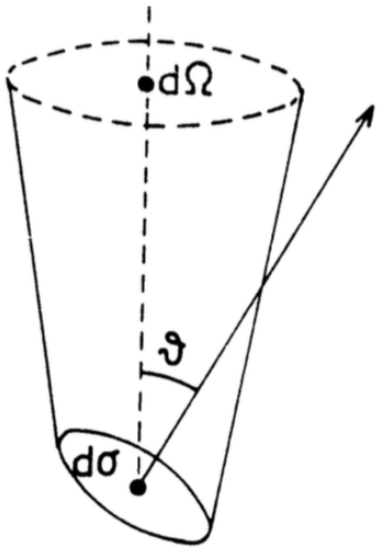

Figure A.3: Illustrative scheme to define the concept of brightness. The figure depicts the geometry that describes the deduction of the quantity I_ν using the infinitesimal parameters $d\sigma$, $d\Omega$, and the angle θ. The infinitesimal surface area in units of cm^2 is denoted by the parameter $d\sigma$, and the angle θ is defined between the normal to $d\sigma$ and the direction to $d\Omega$, where the latter corresponds to the infinitesimal solid angle from the observer's perspective.

It can be inferred from figure A.3 that the infinitesimal power dP passing through the infinitesimal surface area $d\sigma$ follows the following relationship:

$$dP = I_\nu \cos(\theta)\ d\Omega d\theta d\nu\ , \tag{A.17}$$

Where the parameters $d\Omega$, $d\sigma$, and $d\nu$ correspond to the infinitesimal solid angle as seen from the observer, the infinitesimal surface area in units of cm^2, and the infinitesimal bandwidth in units of Hz^{-1}, respectively. Simultaneously, the angle θ is defined between the normal to $d\sigma$ and the direction to $d\Omega$. Finally, the parameter I_ν is defined as specific intensity, brightness, or simply intensity in units of $Wm^{-2}Hz^{-1}sr^{-1}$, where sr denotes the unit of solid angle defined by the Steradian.

By integrating equation A.17 over the entire solid angle Ω that describes the source, we obtain the following:

$$S_\nu = \int_\Omega I_\nu \cos(\theta)\ d\Omega\ , \tag{A.18}$$

This expression is known as the *flux density* S_ν, which refers to the total flux from a source within a certain angle and is in units of $Wm^{-2}Hz^{-1}$.

However, the values obtained for this quantity in the context of radio waves are very small, necessitating the introduction of a new measurement unit, named in honor of the pioneer of Radio Astronomy: the Jansky. Below are the equivalences of this measurement unit, abbreviated as Jy, in conventional unit systems:

$$1Jy = 10^{-26}\ Wm^{-2}Hz^{-1} = 10^{-23}\ erg\ s^{-1}cm^{-2}Hz^{-1}\ . \tag{A.19}$$

It can be observed from the previous expressions that the specific intensity I_ν is an intrinsic quantity of the observed sources, whereas the *flux density* S_ν is a quantity that depends on the distance. Because astronomical sources can exhibit a wide range of intensities across different wavelengths, the Jansky is employed to simplify numbers and facilitate comparisons between various observations.

Appendix B

Clean task products

- **.image**: The main outcome of running the "tclean" task is the primary result image. This image is the result of adding the residual and the model convolved with the clean beam. It contains information such as the source's morphology (extended or compact) and the flux density in units of Jansky (Jy) per beam.
- **.residual:** The residual refers to the emission after subtracting the clean model, generated by selecting regions during the minor cycle of the execution of the *tclean* task. Its units correspond to Jy/beam, but the beam in this image corresponds to a *dirty* one.
- **.model:** clean model from the source, without being convolved. Its units are Jy per pixel (px).
- **.psf:** dirty beam also known as the PSF function.
- **.pb:** This corresponds to the image of normalized sensitivity, which shows concentric circles where the center is displayed in white with a value of one. The importance of this image is associated with the accurate measurement of the flux density of the source of interest. Without performing this type of correction, the measurements would be incorrect.
- **.sumwt:** It is an image of a single pixel, in which there is the addition of the weightings applied. For example, for a *Natural* weight, the sensitivity is equal to the inverse of the root of the sum of the weight.
- **.mom0:** The most common are moment maps: intensity-weighted sums along the velocity axis, in this particular case the emission is weighted for all channels of the data cube and produces images of moment 0 (integrated emission).

Appendix C

Radiative transfer calculation

A concept that is defined when calculating the radiative transfer is the specific intensity (I_ν). This quantity is conserved throughout its path as long as local absorption or emission processes do not take place. The specific intensity is defined as the amount of energy that passes through a surface normal to the path, per unit of time, surface, bandwidth, and solid angle (van der Tak et al. (2007)). The transfer equation for radiation propagated by a differential of area (ds) can then be written as follows:

$$dI_\nu/ds = j_\nu - \alpha_\nu I_\nu, \tag{C.1}$$

where dI_ν is the change in specific intensity [erg^{-1} cm^{-2} Hz^{-1} sr^{-1}], j_ν is the emission coefficient [$ergs^{-1}cm^{-3}Hz^{-1}sr^{-1}$] and α_ν is the absorption coefficient [cm^{-1}]. These two last parameters combined define the source function, defined by:

$$S_\nu = \frac{j_\nu}{\alpha_\nu}. \tag{C.2}$$

When light travels through a medium, it can encounter atoms, molecules, dust particles, and other structures. At each encounter, there is a chance that the photon of light will be absorbed or scattered before continuing on its way. The probability of this occurring depends on the composition of the medium and the frequency of the radiation. How dense the medium is in terms of radiation absorption and scattering is defined as the optical depth τ_ν and is defined as:

$$d\tau_\nu = \alpha_\nu ds. \tag{C.3}$$

Using the definition of optical depth and the source function, we can rewrite the transfer equation as a function of these parameters as:

$$dI_\nu/d\tau_\nu = S_\nu - I_\nu, \tag{C.4}$$

integrating the transfer equation we have that the intensity is defined as:

$$I_\nu(\tau_\nu) = I_0 e^{-\tau_\nu} + \int_0^{\tau_\nu} e^{-(\tau_\nu - \tau_\nu^,)} S_\nu(\tau_\nu^,) d\tau_\nu^, \tag{C.5}$$

where $I_\nu(\tau_\nu)$ is the radiation leaving the medium and I_0 is the background radiation entering the medium. But if the Source function is independent of the location, we can write the radiation as:

$$I_\nu(\tau_\nu) = I_0 e^{-\tau_\nu} + S_\nu(1 - e^{-(\tau_\nu)}). \tag{C.6}$$

Molecular emission refers to the electromagnetic radiation emitted by molecules in interstellar space and the atmospheres of objects such as stars and planets. The study of molecular emission is essential to understanding the composition, temperature, and density of the interstellar medium, as well as to investigating astrophysical processes such as the formation of stars and planets. These molecules absorb energy from different kinds of sources around them, such as stellar or cosmic radiation, and then emit this energy in the form of low-frequency electromagnetic radiation, usually in the microwave or submillimeter range.

These macroscopic absorption and emission phenomena depend directly on coefficients which are defined according to their nature. There are the spontaneous, stimulated emission, and absorption coefficients, as well as excitation or de-excitation coefficients. Therefore, the macroscopic emission as a function of the observed frequency (ν) can be written as:

$$j_\nu = \frac{h\nu_{ul}}{4\pi} n_u A_{ul} \phi_\nu, \tag{C.7}$$

where n_u is the number density of molecules in level u, ϕ_ν is the line profile function depending on line broadening and A_{ul} is the spontaneous emission coefficient.

The macroscopic absorption as a function of the observed frequency (ν) can be written as:

$$\alpha_\nu = \frac{h\nu_{ul}}{4\pi}(n_l B_{lu} - n_u B_{ul})\phi_\nu, \tag{C.8}$$

where B_{ul} is the stimulated emission coefficient and B_{lu} is the absorption coefficient. Now the source function can be written as a function of the Einstein coefficients as follows:

$$S_{\nu ul} = \frac{j_\nu}{\alpha_\nu} = \frac{n_u A_{ul}}{(n_l B_{lu} - n_u B_{ul})} = \frac{2h\nu_{ul}^3}{c^2}\left(\frac{g_u n_l}{g_l n_u} - 1\right)^{-1} \tag{C.9}$$

In thermal equilibrium, the populations of the different energy levels are given by the Boltzmann distribution:

$$\frac{n_u}{n_l} = \frac{g_u}{g_l} e^{-\Delta E_{ul}/kT_{ex}}, \tag{C.10}$$

where g is the degeneracy at the energy level, E is the energy at the level, and introducing the excitation temperature T_{ex} is given by the relative populations of the levels. Even if the excitation is not in thermal equilibrium. Finally, we obtain the specific intensity of a blackbody radiating at T_{ex} as:

$$S_{\nu ul} = B_\nu(T_{ex}). \tag{C.11}$$

In practice, the intensity of the observed target can be represented as C.6. When viewed with a radio telescope, it is viewed from a non-emitting position to remove non-target emission, which is typically the cosmic microwave background emission $I_\nu(0) = I(T_{CMB})$. Therefore, the observed intensity can be written as:

$$I_{\nu obs} = I_\nu(source) - I_\nu(0) = (I_\nu(T_{ex}) - I(T_{CMB}))(1 - e^{-\tau\nu}) \tag{C.12}$$

The Rayleigh-Jeans approximation law describes the spectral distribution of energy radiated by a blackbody at high temperatures in the low-frequency limit. In radio-astronomy, it is possible to determine the brightness of a source by its brightness temperature using this approximation:

$$I_\nu = \frac{2k}{\lambda^2} T_b, \tag{C.13}$$

where the brightness temperature is related to the antenna temperature as:

$$T_b = \frac{T_A}{\eta_A}. \tag{C.14}$$

When the optical depth is very high or the density of the collision partners is very high it can be defined as that the system is in a local thermal equilibrium (LTE) therefore the temperature of the antenna is considered approximately the temperature of excitation and at the same time the kinetic temperature of the gas:

$$T_A \approx T_{ex} \approx T_{kin}. \tag{C.15}$$

Bibliography

Adams F. C., Lada C. J., Shu F. H., 1987, Astrophysical Journal, 312, 788

Adams F. C., Emerson J. P., Fuller G. A., 1990, Astronomical Journal, 357, 606

Alarcón F., et al., 2021, The Astrophysical Journal Supplement Series, 257, 8

Andrews S. M., Wilner D. J., Hughes A. M., Qi C., Dullemond C. P., 2009, The Astrophysical Journal, 700, 1502

Andrews S. M., et al., 2018, The Astrophysical Journal, 869, L41

Armitage P. J., 2017, Physical processes in protoplanetary disks (arXiv:1509.06382)

Arzoumanian D., et al., 2011, Astronomy & Astrophysics, 529, L6

Beckwith S. V. W., Sargent A. I., Chini R. S., Guesten R., 1990a, Astronomical Journal, 99, 924

Beckwith S. V. W., Sargent A. I., Chini R. S., Guesten R., 1990b, Astronomical Journal, 99, 924

Bergin E. A., Du F., Cleeves L. I., Blake G. A., Schwarz K., Visser R., Zhang K., 2016a, The Astrophysical Journal, 831, 101

Bergin E. A., Du F., Cleeves L. I., Blake G. A., Schwarz K., Visser R., Zhang K., 2016b, The Astrophysical Journal, 831, 101

Bergner J. B., Guzmán V. G., Öberg K. I., Loomis R. A., Pegues J., 2018, The Astrophysical Journal, 857, 69

Bergner J. B., Öberg K. I., Bergin E. A., Loomis R. A., Pegues J., Qi C., 2019, The Astrophysical Journal, 876, 25

Bergner J. B., et al., 2021a, The Astrophysical Journal Supplement Series, 257, 11

Bergner J. B., et al., 2021b, The Astrophysical Journal Supplement Series, 257, 11

Bisschop S. E., Jørgensen J. K., van Dishoeck E. F., de Wachter E. B. M., 2007, Astronomy & Astrophysics, 465, 913–929

Bosman A. D., et al., 2021, The Astrophysical Journal Supplement Series, 257, 7

Calahan J. K., et al., 2022, UV-driven Chemistry as a Signpost for Late-stage Planet Formation (arXiv:2212.05539)

Cleeves L. I., Bergin E. A., Harries T. J., 2015, Indirect Detection of Forming Protoplanets via Chemical Asymmetries in Disks (arXiv:1505.07470)

Condon J. J., Ransom S. M., 2016, Essential Radio Astronomy, doi:https://ui.adsabs.harvard.edu/abs/2016era..book.....C.

Dauphas N., Chaussidon M., 2011, Annual Review of Earth and Planetary Sciences, 39, 351–386

Diep P. N., Hoai D. T., Ngoc N. B., Nhung P. T., Phuong N. T., Thai T. T., Tuan-Anh P., 2019, The protoplanetary disc of HD 163296 as observed by ALMA (arXiv:1903.11868)

Dobbs C. L., et al., 2014, Formation of Molecular Clouds and Global Conditions for Star Formation. University of Arizona Press, http://dx.doi.org/10.2458/azu_uapress_9780816531240-ch001

Dullemond C. P., Isella A., Andrews S. M., Skobleva I., Dzyurkevich N., 2020, Astronomy & Astrophysics, 633, A137

Dutrey A., Guilloteau S., Guelin M., 1997, Astronomy and Astrophysics, 317, L55

Dutrey A., et al., 2007, Astronomy & Astrophysics, 464, 615–623

Dutrey A., et al., 2014, Physical and Chemical Structure of Planet-Forming Disks Probed by Millimeter Observations and Modeling. University of Arizona Press, http://dx.doi.org/10.2458/azu_uapress_9780816531240-ch014

Evans N. J., et al., 2009, The Astrophysical Journal Supplement Series, 181, 321

Event Horizon Telescope Collaboration et al., 2019, The Astrophysical Journal Letters, 875, L1

Fairlamb J. R., Oudmaijer R. D., Mendigutía I., Ilee J. D., van den Ancker M. E., 2015, Monthly Notices of the Royal Astronomical Society, 453, 976–1001

Fizeau H., 1867, Annalen der Physik, 208, 292

Flaherty K. M., Hughes A. M., Rosenfeld K. A., Andrews S. M., Chiang E., Simon J. B., Kerzner S., Wilner D. J., 2015, The Astrophysical Journal, 813, 99

Flaherty K. M., et al., 2017, The Astrophysical Journal, 843, 150

Foreman-Mackey D., Hogg D. W., Lang D., Goodman J., 2013, Publ. Astron. Soc. Pac., 125, 306

Fraser H. J., Collings M. P., McCoustra M. R. S., Williams D. A., 2001, Monthly Notices of the Royal Astronomical Society, 327, 1165–1172

Garrido-Deutelmoser J., Petrovich C., Charalambous C., Guzmán V. V., Zhang K., 2023, The Astrophysical Journal Letters, 945, L37

Guzmán V. V., Öberg K. I., Huang J., Loomis R., Qi C., 2017, The Astrophysical Journal, 836, 30

Guzmán V. V., et al., 2021a, The Astrophysical Journal Supplement Series, 257, 6

Guzmán V. V., et al., 2021b, The Astrophysical Journal Supplement Series, 257, 6

Hartmann L., 2001, Accretion Processes in Star Formation, 2nd edn (Cambridge University Press, Cambridge), https://doi.org/10.1017/CBO9780511552090

Hasegawa T. I., Herbst E., 1993, Monthly Notices of the Royal Astronomical Society, 261, 83

Heays A. N., Visser R., Gredel R., Ubachs W., Lewis B. R., Gibson S. T., van Dishoeck E. F., 2014, Astronomy & Astrophysics, 562, A61

Hogg D. W., Bovy J., Lang D., 2010, Data analysis recipes: Fitting a model to data (arXiv:1008.4686)

Huang J., et al., 2017, The Astrophysical Journal, 835, 231

Huang J., et al., 2018, The Astrophysical Journal, 869, L42

Ilee J. D., et al., 2021, The Astrophysical Journal Supplement Series, 257, 9

Isella A., et al., 2016, Physical Review Letters, 117, 251101

Isella A., et al., 2018, The Astrophysical Journal, 869, L49

Jansky K. G., 1933, Nature, 132, 66

Kastner J. H., Qi C., Gorti U., Hily-Blant P., Oberg K., Forveille T., Andrews S., Wilner D., 2015, The Astrophysical Journal, 806, 75

Klaassen P. D., et al., 2013, Astronomy & Astrophysics, 555, A73

Kurtovic N. T., et al., 2018, The Astrophysical Journal, 869, L44

Law C. J., et al., 2021a, The Astrophysical Journal Supplement Series, 257, 3

Law C. J., et al., 2021b, The Astrophysical Journal Supplement Series, 257, 3

Law C. J., et al., 2021c, The Astrophysical Journal Supplement Series, 257, 4

Le Gal R., Brady M. T., Öberg K. I., Roueff E., Petit F. L., 2019, The Astrophysical Journal, 886, 86

Liu S.-F., Jin S., Li S., Isella A., Li H., 2018, The Astrophysical Journal, 857, 87

Michelson A. A., 1920, Proceedings of the National Academy of Science, 6, 474

O'Gorman E., et al., 2020, Astronomy & Astrophysics, 638, A65

Oppenheimer M., Dalgarno A., 1974, Astrophysical Journal, 192, 29

Pinte C., et al., 2018, The Astrophysical Journal, 860, L13

Pokhrel R., et al., 2018, The Astrophysical Journal, 853, 5

Powner M. W., Gerland B., Sutherland J. D., 2009, Nature, 459, 239

Qi C., Wilner D. J., Aikawa Y., Blake G. A., Hogerheijde M. R., 2008, The Astrophysical Journal, 681, 1396–1407

Qi C., Öberg K. I., Wilner D. J., 2013, The Astrophysical Journal, 765, 34

Quirrenbach A., 2009, Experimental Astronomy, 26, 49

Rab C., Kamp I., Dominik C., Ginski C., Muro-Arena G. A., Thi W.-F., Waters L. B. F. M., Woitke P., 2020, Astronomy & Astrophysics, 642, A165

Rucinski S. M., 1985, Astronomical Journal, 90, 2321

Sadavoy S. I., et al., 2014, The Astrophysical Journal Letters, 787, L18

Shakura N. I., Sunyaev R. A., 1973, Astronomy and Astrophysics, 24, 337

Strom K. M., Strom S. E., Edwards S., Cabrit S., Skrutskie M. F., 1989, Astron. J.; (United States), 97

Teague R., 2019, The Journal of Open Source Software, 4, 1632

Teague R., et al., 2016, Astronomy & Astrophysics, 592, A49

Teague R., Bae J., Bergin E. A., Birnstiel T., Foreman-Mackey D., 2018a, The Astrophysical Journal, 860, L12

Teague R., Bae J., Bergin E. A., Birnstiel T., Foreman-Mackey D., 2018b, The Astrophysical Journal, 860, L12

Thompson A. R., Moran J. M., Swenson George W. J., 2017, Interferometry and Synthesis in Radio Astronomy, 3rd Edition, doi:10.1007/978-3-319-44431-4.

Wichittanakom C., Oudmaijer R. D., Fairlamb J. R., Mendigutía I., Vioque M., Ababakr K. M., 2020, Monthly Notices of the Royal Astronomical Society, 493, 234–249

Williams J. P., Cieza L. A., 2011, Annual Review of Astronomy and Astrophysics, 49, 67–117

Wilson T. L., Rohlfs K., Huttemeister S., 2012, Tools of Radio Astronomy, 5th edition, doi:https://ui.adsabs.harvard.edu/abs/2012tra..book.....W.

Yen H.-W., Takakuwa S., Ohashi N., Ho P. T. P., 2013, The Astrophysical Journal, 772, 22

Zhang K., et al., 2021, The Astrophysical Journal Supplement Series, 257, 5

de Gregorio-Monsalvo I., et al., 2013, Astronomy & Astrophysics, 557, A133

van der Tak F. F. S., Black J. H., Schöier F. L., Jansen D. J., van Dishoeck E. F., 2007, Astronomy & Astrophysics, 468, 627–635

Öberg K. I., et al., 2010, The Astrophysical Journal, 720, 480–493

Öberg K. I., Murray-Clay R., Bergin E. A., 2011, The Astrophysical Journal, 743, L16

Öberg K. I., et al., 2021a, The Astrophysical Journal Supplement Series, 257, 1

Öberg K. I., et al., 2021b, The Astrophysical Journal Supplement Series, 257, 1